STRENGTH AND FRACTURE STUDIES OF STEAM TURBINE BLADE

A Thesis Submitted in partial fulfillment of requirement for the award of the degree of

Master of Technology

In

Materials Science and Engineering

Submitted By

Rahul Kaushik
Roll no: 60702013

Under guidence of

Dr. O. P. Pandey
Professer &Head
School of Physics and Material Science
Thapar University,Patiala

SCHOOL OF PHYSICS AND MATERIALS SCIENCES,

THAPAR UNIVERSITY,

PATIALA (PUNJAB)-147004, INDIA

JUNE 2009

CERTIFICATE

This is to certify that the thesis entitled "**Strength and fracture studies of Steam Turbine blade**" submitted by **Mr. Rahul Kaushik** in the partial fulfillment of the requirement for the award of the degree of **M. Tech.** in **Materials Science and Engineering** from the **School of Physics and Materials Science, Thapar University, Patiala (Punjab),** is a record of candidate's own work carried out by him under my supervision and guidance. The matter embodied in this report has not been submitted in part or full to any other university or institute for the award of any degree.

O. Pas

Dr. O.P. Pandey
Professor and Head
School of Physics and Material Science
Thapar University, Patiala

Countersigned by:

O. Pas

Dr. O.P. Pandey
Professor and Head
School of Physics and Material Science
Thapar University, Patiala, Punjab.

R K Sharma 22/7/09

Dr. R.K. Sharma
Dean (Academic Affairs)
Thapar University,
Patiala, Punjab.

ACKNOWLEDGEMENT

I express my deep gratitude and respect to my guide **Dr. O.P. Pandey, Professor and Head, School of Physics and Materials Sciences** for his keen interest and valuable guidance, strong motivation and constant encouragement during the course of work. I thank him from bottom of my heart for introducing me to the field of metallurgy. I thank him for his great patience, constructive criticism and useful suggestions apart from invaluable guidance to me.

I would also like to thank **Dr. K. K. Raina**, **Professor and Deputy Director**, and **Dr. Kulvir Singh**, **Assistant Professor** for his constant guidance and encouragement.

I owe my sincere thanks to all the faculty members of School of Physics and Materials Science for their support and encouragement.

This Thesis could not have been written without the kind help of **Er. S.N.Gosh, Er. M.K. Shau Er. I.D. Kamath, Er. R.D. Sharma, Er. Pradeep Kumar** and all members of Quality assurance, **B.H.E.L. Haridwar**, who has given their support during my experimental work.

I wish to express my warm and sincere thanks to all my friends who devoted their valuable time and helped me in all possible ways towards successful completion of this work.

I owe my most sincere gratitude to my parents whose blessings and honest support give me energy to complete this work successfully. I admire my parent's determination and sacrifice which helps me during the difficult moments of my life, thanks is a very small word for this.

(RAHUL KAUSHIK)

ABSTRACT

Turbines are the key devices for power generation. These are the source for converting the energy into electrical energy. Turbine blades are main component which rotates under fluid flow, which causes the conversion of potential/kinetic energy to convert into electrical energy. The sound stability of the turbine blades is essential to achieve the target. During exposure to adverse condition it may lead to formation of cracks either by corrosion or by erosion. In the present work attempt has been made to locate the cause of failure of the blade of steam turbine. The blade was made of corrosion-resistant high alloy steel of standard grade ASTM A 743 CA 6 NM. In order to do the failure analysis samples were taken from Bharat Heavy Electrical Ltd. Haridwar. The samples were characterized by different characterization techniques like tensile testing, impact testing, hardness testing, chemical analysis, optical microscopy, scanning electron microscopy, energy dispersive spectroscopy, X-ray diffraction technique. Metallographic samples were sectioned from the blade using of cut-off wheel machine (ensuring water cooling during cutting). Five samples were analysed but data of which were taken from three different blades of same turbine are presented. For microstructural examinations, the samples were ground and polished to a mirror like surface by use of metallographic grinding and polishing machines, respectively. The polished samples were etched using Villella's etchant for about 5–15 seconds. For SEM Analysis, the sample was cut from fractured surface of the turbine blade left and the metallographic sample was prepared until polishing stage. Microstructural characterization involved use of scanning electron microscope (SEM) and an optical microscope lined with a computerized image analyzer. By the microscopy we observed that the structure was tempered martensitic. The ductile dimples were confirmed from the scanning electron microscope study. By XRD technique, α iron phase was confirmed. The failure mode was of intergranular type. The material has failed because of inclusion present in it. The details of this analysis are given in the subsequent chapters.

TABLE OF CONTENTS

LIST OF FIGURES

LIST OF TABLES

CHAPTER 1

INTRODUCTION

1. Turbine:

1.1 Introduction:

A turbine is a rotary engine that generates energy from a fluid or air flow. Claude Burdin (1788-1873) coined this term from the Latin turbo, or vortex, during an 1828 engineering competition. Benoit Fourneyron (1802-1867), a student of Claude Burdin, built the first practical water turbine.

The simplest turbine has one moving part, a rotor assembly, which is a shaft with blades attached. Moving fluid acts on the blades, or the blades react to the flow, so that they rotate and impart energy to the rotor. Early turbine examples are windmills and water wheels.

A device similar to a turbine but operating in reverse is a compressor or pump. The axial compressor in many gas turbine engines is a common example.

1.2 Theory of operation:

A working fluid contains potential energy (pressure head) and kinetic energy (velocity head). The fluid may be compressible or incompressible.

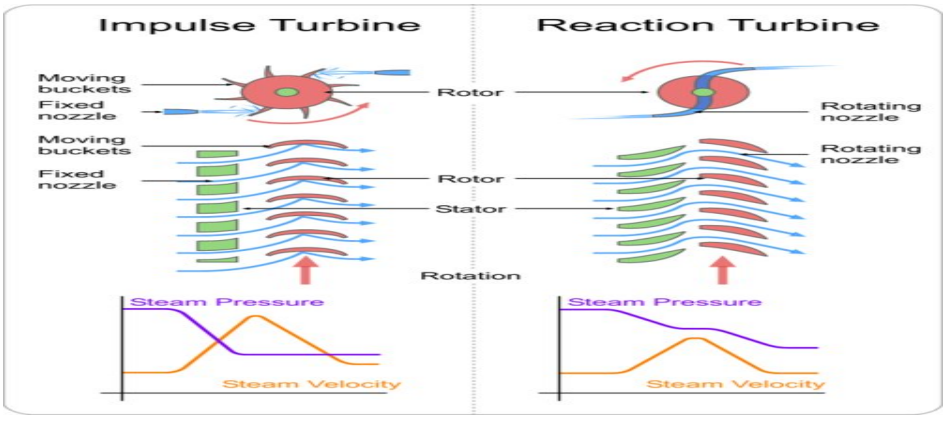

Figure 1.1 working of turbines

1.2.1 Impulse turbines:

These turbines change the direction of flow of a high velocity fluid jet. The resulting impulse spins the turbine and leaves the fluid flow with diminished kinetic energy. There is no pressure change of the fluid in the turbine rotor blades. Before reaching the turbine the fluid's pressure head is changed to velocity head by accelerating the fluid with a nozzle.

1.2.2 Reaction turbines:

These turbines develop torque by reacting to the fluid's pressure or weight. The pressure of the fluid changes as it passes through the turbine rotor blades. A pressure casement is needed to contain the working fluid as it acts on the turbine stage(s) or the turbine must be fully immersed in the fluid flow (wind turbines).

1.3 Types of turbines:

- Steam turbine
- Gas turbine
- Transonic turbine
- Ceramic turbine
- Wind turbine
- Water turbine
    - Pelton turbine, a type of impulse water turbine.
    - Francis turbine, a type of widely used water turbine.
    - Kaplan turbine, a variation of the Francis Turbine.
    - Voith, water turbine.

1.4 Steam turbine:

A steam turbine is a mechanical device that extracts thermal energy from pressurized steam, and converts it into rotary motion. Its modern manifestation was invented by Sir Charles Parsons in 1884 [1].

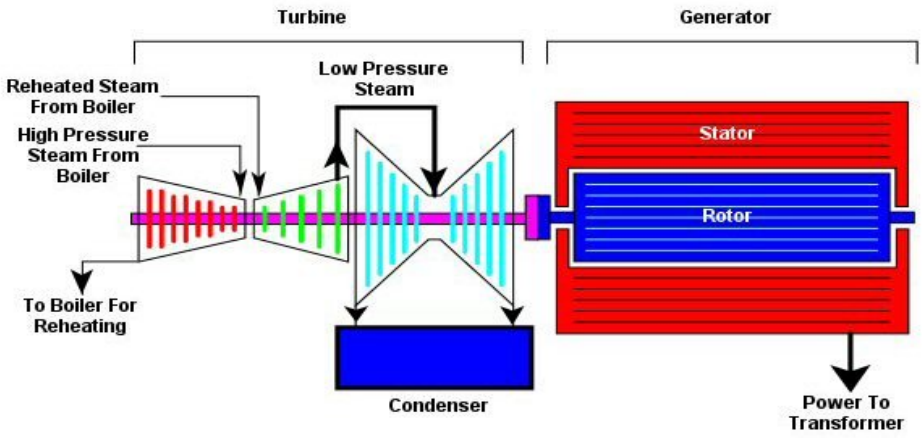

Figure 1.2 Steam turbine

It has almost completely replaced the reciprocating piston steam engine (invented by Thomas Newcomen and greatly improved by James Watt) primarily because of its greater thermal efficiency and higher power-to-weight ratio. Because the turbine generates rotary motion, it is particularly suited to be used to drive an electrical generator – about 80% of all electricity generation in the world is by use of steam turbines. The steam turbine is a form of heat engine that derives much of its improvement in thermodynamic efficiency through the use of multiple stages in the expansion of the steam, which results in a closer approach to the ideal reversible process.

1.4.1 History:

The first device that may be classified as a reaction steam turbine was little more than a toy, the classic Aeolipile, described in the 1st century by Hero of Alexandria in Roman Egypt [2,3,4]. More than a thousand years later, the first impact steam turbine with practical applications was invented in 1551 by Taqi al-Din in Ottoman Egypt, who described it as a prime mover for rotating a spit. Similar smoke jacks were later described by John Wilkins in 1648 and Samuel Pepys in 1660. Another steam turbine device was created by Italian Giovanni Branca in 1629 [5].

The modern steam turbine was invented in 1884 by the Englishman Sir Charles Parsons, whose first model was connected to a dynamo that generated 7.5 kW of electricity [6]. The invention of Parson's steam turbine, which made cheap and plentiful electricity possible and revolutionised marine transport and naval warfare in the world[7]. His patent was licensed and the turbine

scaled-up shortly after by an American, George Westinghouse. A number of other variations of turbines have been developed that work effectively with steam. The de Laval turbine (invented by Gustaf de Laval) accelerated the steam to full speed before running it against a turbine blade. This was good, because the turbine is simpler, less expensive and does not need to be pressure-proof. It can operate with any pressure of steam. It is also, however, considerably less efficient. The Parson's turbine also turned out to be relatively easy to scale-up. Parsons had the satisfaction of seeing his invention adopted for all major world power stations. The size of his generators had increased from his first 7.5 kW set up to units of 50,000 kW capacity. He knew that the total output from turbo-generators constructed by his firm C. A. Parsons and Company and by their licensees, for land purposes alone, had exceeded thirty million horse-powers [8]. Within Parson's lifetime the generating capacity of a unit was scaled-up by about 10,000 times [9].

1.4.2 Principle of Operation and Design:

An ideal steam turbine is considered to be an isentropic process, or constant entropy process, in which the entropy of the steam entering the turbine is equal to the entropy of the steam leaving the turbine. No steam turbine is truly “isentropic”, however, with typical isentropic efficiencies ranging from 20%-90% based on the application of the turbine. The interior of a turbine comprises of several sets of blades, or “buckets” as they are more commonly referred to. One set of stationary blades is connected to the casing and one set of rotating blades is connected to the shaft. The sets intermesh with certain minimum clearances, with the size and configuration of sets varying to efficiently exploit the expansion of steam at each stage.

1.5 Corrosion-Resistant High-Alloy Steels:

1.5.1 Introduction:

Corrosion-resistant high-alloy cast steels, more commonly referred to as cast stainless steels; have grown steadily in technological and commercial importance during the past 40 years. The principal applications for these steels are as materials of construction for chemical-processing and power generating equipment involving corrosion service in aqueous or liquid-vapour environments at temperatures normally below 315 °C (600 °F). These alloys are also used for special services at temperatures to 650 °C (1200 °F). An appropriate definition for cast stainless

steels is the familiar one based on the discovery in 1910 that a minimum of 12% Cr will impart resistance to corrosion and oxidation to steel [10].

Cast stainless steels are defined as ferrous alloys that contain a minimum of 12% Cr for corrosion resistance. Most cast stainless steels are of course considerably more complex compositionally than this simple definition implies. Stainless steels typically contain one or more alloying elements in addition to chromium (for example, nickel, molybdenum, copper, niobium, and nitrogen) to produce a specific microstructure, corrosion resistance, or mechanical properties for particular service requirements. Corrosion-resistant high-alloy cast steels are usually classified on the basis of composition or microstructure. It should be recognized that these bases for classification are not completely independent in most cases; that is, classification by composition also often involves microstructural distinctions.

Table 1.1 lists the compositions of the commercial cast corrosion-resistant alloys. Alloys are grouped as chromium steels, chromium-nickel steels in which chromium is the predominant alloying element, and nickel-chromium steels in which nickel is the predominant alloying element. The service-ability of cast corrosion-resistant steels depends greatly on the absence of carbon, and especially precipitated carbides, in the alloy microstructure. Therefore, cast corrosion-resistant alloys are generally low in carbon (typically <0.08% C).

Table 1.1 Compositions and microstructures of corrosion-resistant high-alloy cast steels

Alloy CA-6 NM (Cromium-Nickle)

Microstructure Tempered Martensitic

Composition, %	Cr	Ni	Mo	Si	Mn	P	S	C
	11.5-14.0	3.5-4.5	0.40-1.0	1.00	1.00	0.04	0.03	0.06

Martensitic grades include Alloys CA-15, CA-40, CA-15M, and CA-6NM. The CA-15 alloy contains the minimum amount of chromium necessary to make it essentially rustproof. It has good resistance to atmospheric corrosion as well as too many organic media in relatively mild service. A higher-carbon modification of CA-15, CA-40 can be heat treated to higher strength

and hardness levels. Alloy CA-15M is a molybdenum-containing modification of CA-15 that provides improved elevated-temperature strength. Alloy CA-6NM is an iron-chromium-nickel molybdenum alloy of low carbon content.

1.5.2 Mechanical Properties:

Strength and Hardness. Representative room-temperature tensile properties, hardness, and Charpy impact values for corrosion-resistant alloys are given in Table 2. These properties are representative of the alloys rather than the specification requirements. Minimum specified mechanical properties for these alloys are given in ASTM standards A 351, A 743, A 744, and A 747. A wide range of mechanical properties are attainable in high-alloy steel grades, depending on the selection of alloy composition and heat treatment. Tensile strengths ranging from 476 to 1310 MPa (69 to 190 ksi) and hardnesses from 130 to 400 HB are available among the cast corrosion-resistant alloys. Similarly, wide ranges exist in yield strength, elongation, and impact toughness.

Table 1.2 Room-temperature mechanical properties of cast corrosion-resistant alloys

Alloy	CA-6NM
Heat treatment	>955 °C, Air Cool, Tempring
Tensile Strength	827 MPa
Yield strength (0.2% offset)	689 MPa
Elongation in 50 mm (2 in.), %	24
Reduction in area, %	60
Hardness, (HB)	269
Charpy impact energy	94.9 J

The straight chromium steels (CA-15, CA-40, CB-30, and CC-50) possess either martensitic or ferritic microstructures in the end-use condition (Table 1). The CA-15 and CA-40 alloys, which contain nominally 12% Cr, are hardenable through heat treatment by means of the martensite

transformation and are often selected as much or more for their high strength as for their comparatively modest corrosion resistance. Castings of these alloys are heated to a temperature at which the structure is fully austenitic and then cooled at a rate (usually in air) adapted to the casting composition so that the austenite transforms to martensite. Strengths in this condition are quite high (for example, 1034 to 1379 MPa, or 150 to 200 ksi), but tensile ductility and impact toughness are limited. Consequently, martensitic castings are usually tempered at 315 to 650 °C (600 to 1200 °F) to restore ductility and toughness at some sacrifice in strength. It follows, then, that significant ranges of tensile properties, hardness, and impact toughness are possible with the martensitic CA-15 and CA- 40 grades, depending on the choice of tempering temperature.

The higher-chromium CB-30 and CC-50 alloys, on the other hand, are fully ferritic alloys that are not hardenable by heat treatment. These alloys are generally used in the annealed condition and exhibit moderate tensile properties and hardness (Table 1.2). Like most ferritic alloys, CB-30 and CC-50 possess limited impact toughness, especially at low temperatures. Three chromium-nickel alloys--CA-6NM, CB-7Cu, and CD-4MCu--are exceptional in their response to heat treatment and the resultant mechanical properties. Alloy CA-6NM is balanced compositionally for martensitic hardening response. This alloy was developed as an alternative to CA-15 and has improved impact toughness and weldability. The CB-7Cu and CD-4MCu alloys both contain copper and can be strengthened by age hardening. These alloys are initially solution heat treated and then cooled rapidly (usually by quenching in oil or water); thus, the phases that would normally precipitate at slow cooling rates cannot form. The casting is then heated to an intermediate aging temperature at which the precipitation reaction can occur under controlled conditions until the desired combination of strength and other properties is achieved. The CB-7Cu alloy possesses a martensitic matrix, while the CD-4MCu alloy possesses a duplex microstructure, consisting of approximately 40% austenite in a ferritic matrix. Alloy CB-7Cu is applied in the aged condition to obtain the benefit of its excellent combination of strength and corrosion resistance, but alloy CD-4MCu is seldom applied in the aged condition, because of its relatively low resistance to SCC in this condition compared to its superior corrosion resistance in the solution-annealed condition.

The CE, CF, CG, CH, CN, and CK alloys are essentially not hardenable by heat treatment. To ensure maximum corrosion resistance, however, it is necessary that castings of these grades

receive a high-temperature solution anneal. This treatment consists of holding the casting at a temperature that is high enough to dissolve all chromium carbides, which are damaging to intergranular corrosion resistance, and then cooling them rapidly enough to avoid reprecipitation of the carbides by quenching in water, oil, or air. Although this can be accomplished throughout in the lower-carbon grades (<0.08% C), heavy sections of alloys with higher carbon contents may have carbides present at some distance below the surface where the cooling rate is slow. Subsurface carbides could be exposed by subsequent machining of the casting, resulting in lowered corrosion resistance in service. By virtue of their microstructures, which are fully austenitic or duplex without significant carbide precipitation, the alloys exhibit generally excellent impact toughness at low temperatures. The tensile strength range represented by these alloys typically extends from 476 to 669 MPa (69 to 97 ksi). As indicated earlier in this article, the alloys with duplex structures can be strengthened by balancing the composition for higher ferrite levels. The tensile and yield strength of CF alloys with a ferrite number of 35 are typically 150 MPa (22 ksi) higher than those of full austenitic alloys.

Fatigue properties can become a design factor in applications in which the casting experiences cyclic loading conditions in service. The resistance of cast stainless steels to fatigue depends on a sizable number of material, design, and environmental factors. For example, design factors of importance include the stress distribution within the casting (residual and applied stresses), the location and severity of stress concentrators (surface integrity), and the environment and service temperature. Material factors of importance include strength and microstructure. It is generally found that fatigue strength increases with the tensile strength of a material. Both fatigue strength and tensile strength generally increase with decreasing temperature. Under equivalent conditions of stress, stress concentration, and strength, evidence suggests that austenitic materials are less notch sensitive than martensitic or ferritic materials.

Toughness. The fully austenitic corrosion-resistant alloys and those with duplex microstructures exhibit excellent toughness. the magnitude of toughness attainable in various grades in Charpy keyhole impact testing.

Effects of Aging. Cast corrosion-resistant high-alloy steels are extensively used at moderately elevated temperatures (up to 650 °C, or 1200 °F). Elevated-temperature properties are important selection criteria for these applications. In addition, room-temperature properties after service at

elevated temperatures are increasingly considered because of the aging effect that these exposures may have. For example, cast alloys CF-8C, CF-8M, CE-30A, and CA-15 are currently used in high-pressure service at temperatures to 540 °C (1000 °F) in sulfurous acid environments in the petrochemical industry. Other uses are in the power-generating industry at temperatures to 565 °C (1050 °F). Room-temperature properties in the aged condition, that is, after exposure to elevated service temperatures, may differ from those in the as-heat-treated condition because of the microstructural changes that may take place at the service temperature. Microstructural changes in iron-nickel-chromium-(molybdenum) alloys may involve the formation of carbides and such phases as σ, χ, and η(Laves). The extent to which these phases form depends on the composition as well as the time at elevated temperature.

The martensitic alloys CA-15 and CA-6NM are subject to minor changes in mechanical properties and SCC resistance in NaCl and polythionic acid environments upon exposure for 3000 h at up to 565 °C (1050 °F). In CF-type chromiumnickel-(molybdenum) steels, only negligible changes in ferrite content occur during 10,000 h exposure at 400 °C (750 °F) and during 3000 h exposure at 425 °C (800 °F). Carbide precipitation, however, does occur at these temperatures, and noticeable Charpy V-notch energy losses have been reported.

Above 425 °C (800 °F), microstructural changes in chromium-nickel-(molybdenum) alloys take place at an increased rate. Carbides and σ phase form rapidly at 650 °C (1200 °F) at the expense of ferrite. Tensile ductility and Charpy V-notch impact energy are prone to significant losses under these conditions. Density changes, resulting in contraction, have been reported as a result of these high-temperature exposures.

1.5.3 Heat Treatment:

Alloy CA-6NM (UNS J91540) possesses better casting behaviour and improved weldability, it equals or exceeds all of the mechanical, corrosion, and cavitation resistance properties of CA-15, and it has largely replaced the older alloy. Both CA- 6NM and CA-15 castings are normally supplied in the normalized condition at 955 °C (1750 °F) minimum and tempered at 595 °C (1100 °F) minimum. However, when it is necessary or desirable to anneal CA-6NM castings, a

temperature of 790 to 815 °C (1450 to 1500 °F) should be used. The alloy should be furnace cooled or otherwise slow cooled to 595 °C (1100 °F), after which it can be air cooled. When stress relieving is required, CA-6NM can be heated to 620 °C (1150 °F) maximum, followed by slow cooling to prevent martensite formation.

Martensitic alloys. Alloy CA-6NM should be hardened by air cooling or oil quenching from a temperature of 1010 to 1065 °C (1850 to 1950 °F). Even though the carbon content of this alloy is lower than that of CA-15, this fact in itself and the addition of molybdenum and nickel enable the alloy to harden complete. The choice of cooling medium is primarily determined by the maximum section size. Section sizes exceeding 125 mm (5 in.) will harden completely when cooled in air. Alloy CA-6NM is not susceptible to cracking during cooling from elevated temperatures. For this reason, no problem should arise in the air cooling or oil quenching of configurations that include thick as well as thin sections. A wide selection of mechanical properties is available through the choice of tempering temperatures. Alloy CA-6NM is normally supplied, normalized, and tempered at 595 to 620 °C (1100 to 1150 °F). Reaustenitizing occurs upon tempering above 620 °C (1150 °F); the amount of reaustenitization increases with temperature. Depending on the amount of thisy without significant austenite retention when cooled as suggested. Transformation, cooling from such tempering temperatures may adversely affect both ductility and toughness through the transformation to untempered martensite.

1.5.4 Applications of C-Type Alloys:

Martensitic grades include CA-15, CA-40, CA-15M, and CA-6NM. Alloy CA-15 contains the minimum amount of chromium necessary to make it essentially rustproof. It has good resistance to atmospheric corrosion as well as too many organic media in relatively mild service. Alloy CA-40 is a higher-carbon modification of CA-15 that can be heat treated to higher strength and hardness levels. A molybdenum-containing modification of CA-15, alloy CA-15M provides improved elevated-temperature strength properties. Alloy CA-6NM is an iron-chromium-nickel-molybdenum alloy of low carbon content. The presence of nickel offsets the ferritizing effect of the low carbon content so that strength and hardness properties are comparable to those of CA-15 and impact strength is substantially improved. The molybdenum addition improves the resistance of the alloy in seawater. A wide range of mechanical properties can be obtained in the martensitic alloy group. Tensile strengths from 620 to 1520 MPa (90 to 220 ksi) and hardnesses

as high as 500 HB can be obtained through heat treatment. The alloys have fair to good weldability and machinability if proper techniques are employed; CA-40 is considered the poorest and CA-6NM is the best in this regard. The martensitic alloys are used in pumps, compressors, valves, hydraulic turbines, propellers, and machinery components.

CHAPTER 2
LITRETURE REVIEW

2. Fracture:

2.1 Introduction:

Fracture is a form of failure and is defined as separation or fragmentation of solid body into two or more parts under the action of stress, at temperature below the melting point. The process of fracture can be considered to be made up of two components crack initiation and crack propagation. Fracture can occur under all service conditions. Material subjected to alternating or cyclic loading fail due to fatigue. The fracture under such circumstances is called fatigue fracture.

Depending on the ability of material to undergo plastic deformation before the fracture two fracture modes can be defined, these are ductile and brittle fracture.

Figure 2.1 Illustrating fracture

2.1.1 Ductile:

It is characterized by appreciable amount of plastic deformation prior to propagation of the crack. It is characterized by extensive plastic deformation ahead of crack tip. Crack growth is stable and resists further extension unless applied stress is increased. Ductile material can absorb shock or energy (during the deformation) before failure. It occurs in most metals which are not

too cold. FCC metals are usually ductile because of the presence of large number of active slip systems. The surface topography of ductile failure is cup and cone type.

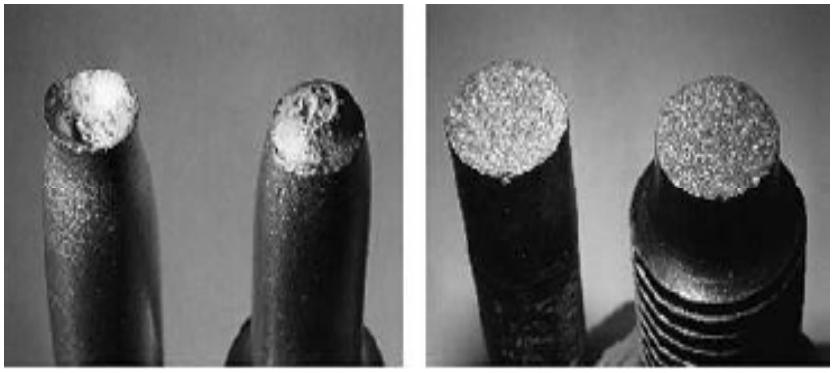

. Ductile fracture Brittle fracture

Figure 2.2 Illustrating types of fracture.

2.1.2 Brittle:

It is characterized by rapid rate of crack propagation with negligible plastic deformation. Crack propagates by cleavage nearly perpendicular to direction of applied stress with breaking of atomic bonds along specific crystallographic plane (cleavage plane). It is caused by decreasing temperature, increasing strain rate, triaxial stress condition. Less amount of energy absorption occurs before fracture. It occurs mostly in cold metals and ceramics. BCC and HCP metals are susceptible to brittle fracture because there are very less number of active slip planes or slip systems for plastic deformation.

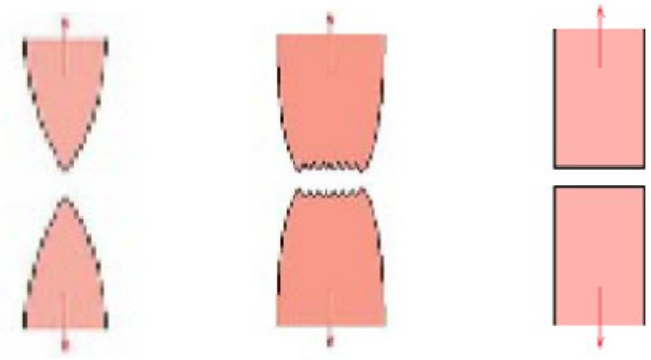

Highly ductile fracture Moderately ductile fracture, Brittle fracture

eg. Pure gold eg. Most metals

Figure 2.3 Illustrating crack propagation

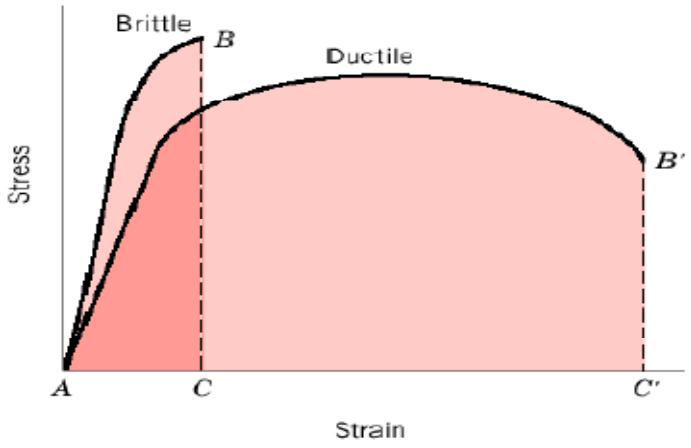

Figure 2.4 represents the degree of plastic deformation exhibited by both brittle and ductile materials before fracture.

2.2 Basics of Ductile Fracture:

The ductile fracture can be divided into three categories:

2.2.1 Shear failure:

It occurs as a result of extensive slip on active slip planes. It is characterized by slip on successive basal planes until the crystal separate by shear. It is observed mainly in HCP metals like magnesium.

Figure 2.5 Ductile fracture by shear failure

2.2.2 Complete ductile failure:

Slip occurs in failure by slipping is common phenomenon. Slip planes in case of polycrystalline materials until it is drawn to a point before rupture. It happens in case of very ductile and pure materials like gold and lead.

Figure 2.6 Complete Ductile failure

2.2.3 Cup & cone type failure:

Fracture begins at the centre of the specimen by the mechanism of void nucleation, growth and coalescence followed failure by shearing along the shear planes to form the cup and cone type failure.

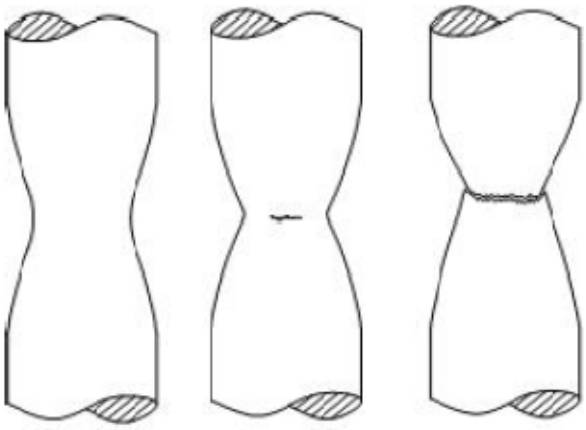

Figure 2.7 Cup & cone failure

Ductile fracture in engineering material is normally preceded by extensive plastic deformation that occurs by slow tearing of metal with considerable expenditure of energy. Ductile fracture in tension usually occurs after a localized reduction in diameter called necking. It begins to neck beyond the ultimate tensile strength, which is the maximum point in the load-elongation curve. Necking begins at the point of plastic instability where the increase in strength due to strain hardening fails to compensate for the decrease in cross sectional area which occurs at the maximum load. The formation of necking introduces tri-axial state of stress in this region. A hydrostatic component of tension acts at the centre of the necked region. Many fine cavities form in this region and under continues straining tends to grow in size and finally coalesced. The void coalescence is synonymous with the crack formation. The crack initiates near the centre of the neck (minimum area), which propagates in a zigzag fashion, until it undergoes a large zig to the surface to form the cup the cone of the cup-cone fracture.

2.3 Dimple Rupture:

When overload is the principal cause of fracture, most common structural alloys fail by a process known as microvoid coalescence. The microvoids nucleate at regions of localized strain discontinuity, such as that associated with second phase particles, inclusions, grain boundaries, and dislocation pile-ups. As the strain in the material increases, the microvoids grow, coalesce, and eventually form a continuous fracture surface. This type of fracture exhibits numerous cuplike depressions that are the direct result of the microvoid coalescence. The cuplike depressions are referred to as dimples, and the fracture mode is known as dimple rupture [11].

The size of the dimple on a fracture surface is governed by the number and distribution of microvoids that are nucleated. When the nucleation sites are few and widely spaced, the microvoids grow to a large size before coalescing and the result is a fracture surface that contains large dimples. Small dimples are formed when numerous nucleating sites are activated and adjacent microvoids join (coalesce) before they have an opportunity to grow to a larger size. Extremely small dimples are often found in oxide dispersion strengthened materials.

Dimple shape is governed by the state of stress within the material as the microvoids form and coalesce. Fracture under conditions of uniaxial tensile load results in the formation of essentially

equiaxed dimples bounded by a lip or rim. Depending on the microstructure and plasticity of the material, the dimples can exhibit a very deep, conical shape or can be quite shallow. The formation of shallow dimples may involve the joining of microvoids by shear along slip bands [12].

Metals that undergo considerable plastic deformation and develop large dimples frequently contain deformation markings on the dimple walls. These markings occur when slip-planes at the surface of the dimples are favorably oriented to the major stress direction. The continual straining of the free surfaces of the dimples as the microvoids enlarge produces slip plane displacement at the surface of the dimple [13].

The fracture on the blade in an aircraft gas turbine has been studied to see the cause of crack initiation [14]. The turbine blades were made of Ni-base superalloy of MAR 200 Hf grade and fabricated by DS investment casting. From the visual examination of the fractured surface, the turbine blade had initially cracked by a fatigue mechanism over a period of time and then fractured by the overload at the last moment. Further examination, the crack initiated at the trailing edge of the blade, and propagated by the fatigue under the cyclic loading experienced by the blade during service. The pores and segregated area of Hf and Ti at the trailing edge of the blade, caused by DS investment casting, is found by the microstructure and EDX analysis of the blade. The crack initiated at this area and was due to the stress concentration at the pores and segregation of Hf and Ti [14].

The failed gas-turbine blades were sectioned for metallographic investigations. The material properties and behavior at high temperature were interpreted on the basis of the observed microstructures and the phases present in the alloy. The interpretations were related to the operating conditions of the turbine blade; and main cause of failure was found to be creep damage. It is concluded that the trailing edge (transverse cross-section) of the blade failed by creep damage. Hence, it is not at all safe to continue to use the blade in the gas-turbine engine in the power plant. It is recommended that more efficient blade cooling and/or thermal barrier coatings should be applied to the turbine blades. In particular, the quality of the TBC must be assured in the transverse-section at the trailing edge of the blade. Alloy composition for the

blades should be readjusted to ensure that the columbium (Cb) content be at least 2% in the superalloy so as to avoid c'-particle coarsening in the microstructure. It is suggested to ensure that the grain boundaries in the new directionally solidified blades should be well parallel to each other and perfectly aligned along the blade axis; this would ensue avoiding the creep damage by cavities at grain boundaries [15].

An analysis of the cause of fracture in a steam turbine blade root was investigated by Kubiak et al [16]. The metallurgical investigation revealed that the crack was propagated by a combined process corrosion-fatigue. The analysis concludes that the metallurgical mode of the blade root failure was the corrosion-fatigue at the zone of the highest stress concentration caused by mismatch and errors in the installation between the blade root platform and the rotor fastening tree. Also, the crack was propagated by the vibrations around of the first mode of vibration [16].

The fracture of LPT1 blade which caused the in-flight shutdown event initiated from a V-shape notch defect. The failure mechanism of this blade was fretting fatigue for there were conditions of fretting wear and some fretting pits and cracks were visible [17].

A 150MW gas turbine experienced a forced break down because of extremely high vibrations and subsequent output power reduction down to almost zero [18]. Before the break down, the turbine was operated by approximately 1800 hours in intermittent mode, with a record of 65 start-ups in total. When the turbine casing was opened it was found that all blades, stationary and moving ones, were in damaged status. Especially destroyed was the first row moving blades, with four missing blades. In contrast, no damage or excessive wearing out was found neither in the combustion chamber nor in the transition pieces; even nor at the region of entry to the nozzles. The results of further investigation lead to establish that the former cause of the blade failure was low cycle fatigue that originated a crack in the securing pin hole (stress raiser) located at the root of the blade and propagated [18].

A last stage (L-0) turbine blades failure was experienced at a 28 MW geothermal unit after seven years of operation period [19]. This unit has one flow intermediate/low-pressure turbine composed of nine stages with 25-in./3600 rpm last stage blades. The last stage row contains 62

free standing blades. Visual examination indicated that the 37 L-0 blades had cracks in their airfoils initiating at the trailing edge, near the blade platform Based on the analysis of results from the last stage blade metallographic examination, unit operational parameters, blade natural frequencies and blade stresses, it may be concluded that L-0 blade failure initiation and propagation was driven by a high cycle fatigue mechanism accelerated in high degree by erosion/corrosion processes in the blade trailing edge zone [19].

The cause of the engine damage due to the fracture of the J85 Engine first stage turbine blades was investigated [20]. Discoloration due to thermal effect and fine multi-cracks as well as necking at 1/3 of the way down from the tip on the entire first stage turbine blade concave side surface have been noted. Of the first stage blades, nine had fractures 1/3 of the way down from the tip, and at the fractured location more severe necking has been found than blades without fracture. As a result of observing the fine texture of fractured blades and the blades where deformation has occurred, wedge-type intergranular cracks and TCP phase as well as carbide phase have been identified, and γ deformation and depletion found around the fracture surface. There were no traces of thermal damage to the first stage vane, no IOD phenomenon has been noted. Analysis of turbine blade deformation and fracture profile and microstructural deformation phenomenon determined that blade fracture was due to high temperature creep rupture [20].

The failure of a second stage blade in a gas turbine was investigated that serious pitting was occurred on the blade surfaces and there were evidences of fatigue marks in the fracture surface. The microstructural changes were not critical. It was found that the crack initiated by the hot corrosion from the leading edge and propagated by fatigue and finally, as a result of the reduction in cross-section area, fracture was completed [21].

The failure analysis of gas turbine blades made of nickel-base alloy was carried out [22]. The microstructural investigation of the blades revealed the presence of continuous and dispersed films of carbides in grain boundaries and coarsened γ' precipitates resulting from exposure to extreme temperatures and subsequent operation. There were a large number of cracks at different regions of blades because of operation at high temperatures and stresses for a long period of

time. An intergranular crack was found on the failed blade coating; there were some micro-cavities on the fracture surface that served as the origin of a creep failure mechanism; there were several intergranular cracks on transverse section of the first stage blade surface. Also, due to operation at high temperatures, many annealing twins were observed [22].

Cracking of blade fingers occurred in a few numbers of low pressure 1st stage blades for a certain type of steam turbines [23]. The cracking of the blade finger has been caused by the high cycle fatigue, and surface defect coming from rough machining induces the initiation of crack. Resonance of second type axial vibratory mode with nozzle passing frequency was the source of high cycle fatigue load. Based on the mechanism investigation of the blade fractures, the blade group has been modified into 10 blades per group without any change of vane and dovetail to avoid resonant vibration. The new blades have been operated safely more than 2 years since the design modification. The research also demonstrates resonance of second group axial modes with nozzle passing frequency is dangerous for blade groups, and it is better to avoid such resonance. Changing the number of blades in the blade group is an effective way to adjust the natural frequency to avoid axial mode resonance [23].

A failure investigation has been conducted on the turboblades used in a locomotive turbocharger [24]. These blades are made from as-cast K418 nickel-base (Ni-base) superalloy. Fracture occurred at the mid-airfoil and tip locations. In the mid-airfoil regions, a high density of intergranular cracks and dent marks are present. The microstructure at the mid-airfoil is typical of overheat damage, such as melting of the boundary or interdendritic region and degraded interdendritic carbides and remelting of eutectic phases. The fracture surfaces of the failed blades have a dendritic appearance without evidence of fatigue features. It is suggested that these fractures were formed instantaneously. Overheat damage made the strength in interdendritic region decrease so that microcracking occurred preferentially in the interdendritic region. Under the action of bending stress and the spin centrifugal tensile stress, the microcracks propagated within the interdendritic region and converged so that the transverse fracture occurred at the mid-airfoil location where the maximum stress acted. The fragments from previously fractured blades hit neighboring blades, ultimately causing damage to all the turboblades [24].

Failure case of the low pressure blades of steam turbine is presented in reference [25]. The suction side of blades has been quenched to improve the erosion resistance. Cracks with different lengths were found in the quenched region of final stage blades. The failure analysis of blades was performed in terms of composition analysis, microstructure and mechanical tests, etc. The yield strength and tensile strength conform to the corresponding standard, whereas the elongation, area reduction and impact toughness are lower than the criteria. From the crack morphology, fractography and composition analysis on the fracture surface, it was found that the failure mechanism of blades is the environment assisted fatigue fracture. The location of fatigue crack initiation is related with the salient of blades due to the stress concentration. In order to decrease the blade cracking susceptibility, the increment of tempered temperature in both modified treatment and high-frequency hardening was recommended [25].

The failure process of the compressor blades was investigated using experimental characterization methods [26]. The experimental results showed no metallurgical and mechanical defects for the blade materials. Microstructures of the blade root and airfoil as well as the hardness and tensile properties were all comparable with those reported in the standard specification AMS 4928Q. Fractography experiments showed clearly multiple crack initiation sites and fatigue beach marks. Debris particles were observed on the fracture surface of samples and in the mouth of initiated cracks. The blade surface in contact to the disc in the dovetail region showed a higher surface roughness than the other surfaces. Based on the results obtained, the fretting fatigue mechanism was proposed for the premature failures. It was concluded that the stress concentration has been caused by either unsuitable curvature ratio of the disk dovetail, incorrect design of the blade or insufficient distance between the blade root and the disk in dovetail region. Multiple crack initiation and growth was observed in this failure due to fretting fatigue mechanism. Crack initiation was occurred at the corner on contact facet of blade dovetail between blade dovetail and wheel dovetail. It was concluded that the stress concentration has been caused by either unsuitable curvature ratio of the disk dovetail, incorrect design of the blade or insufficient distance between the blade root and the disk in dovetail region [26].

A case study of failure analysis of a 40 MW gas turbine blade made of Udimet 500 has been investigated [27]. The cause of failure is found to be intergranular cracks which started during

exposure to high temperature. The cracks initiated from the grain boundaries and propagated to the critical length to result in catastrophic fracture. In many locations M6C type secondary carbides were found agglomerated on grain boundaries. Also micro-cavities were found on fracture surfaces which served as an origin of creeping failure mechanism [27].

The failure analysis of twelve percent chromium martensitic stainless steel blades of the medium-pressure stage of a thermoelectric centre turbo-blower was presented which brakes during use [28]. The results indicated that at least one of the blades of the medium pressure stage failed by a corrosion-fatigue mechanism, whose nucleation was associated with the presence of corrosion pits on its suction side. The high-pressure blades presented hardness bellow the specification and presence of corrosion pits and cracks [28].

An another study of failure of turbine blade indicate environmental effect [29]. The fracture initiated from a cavity caused by erosion. The erosion of the trailing edge is not normal, but can occur during prolonged operation on the partial load. Additionally, NaCl corrosion may have contributed to the failure located at the trailing edge of the blade. The time required for the blade to fracture by high-cycle fatigue after it was freed from the blade group was estimated to be about 10 min [29].

The failure of a LP (low pressure) turbine blade of a 220 MW thermal power plant is presented in reference [30]. The blade was made of martensitic stainless steel and the structure was tempered martensite. There was no evidence of degradation of blade material. The fracture took place at the aerofoil region, 113-mm from the root. Throughout the blade surface Si rich phases were detected. Several pits/grooves were found on the edges of the blades and chloride was detected in these pits. These were responsible for the crevice type corrosion. The probable carriers of Cl were Ca and K, which were found on the blade. The failure mode was intergranular type. Possibly the ultimate failure was due to corrosion-fatigue [30].

The fracture of a turbojet engine turbine blade was investigated by Park et al [31]. Visual and surface examination showed that the turbine blade had initially cracked by a fatigue mechanism over a period of time and then failed by overload at the last moment. The fatigue crack initiated

on a surface damaged by rubbing. Also the cracked turbine blade was severely damaged by hot gas flow and discolored. This heat damage made the gamma prime phase in the matrix (Ni-base super alloy) coarsen and lowered the fatigue strength of the base material assisting to the premature fatigue fracture. The decrease of the strength of the material due to degradation of gamma prime phase was verified by hardness measurements. The possible relevance of other parts attached to the engine shaft to the fracture was reviewed. From this review it is inferred that the root cause of cracking and excessive heat damage might be attributed to eccentricity of the shaft resulting from various reasons—shaft misalignment, uneven wear of bearing elements and mismatch in clearance, etc. However this is an assumption that should be verified by positive supporting evidence from condition monitoring of engines [31].

CHAPTER 3

EXPERIMENTAL PROCEDURE

3. Introduction:

In this chapter all the details about the preparation and characterization of samples has been described. The experimental techniques involve following steps:

PROCESS FLOW CHART

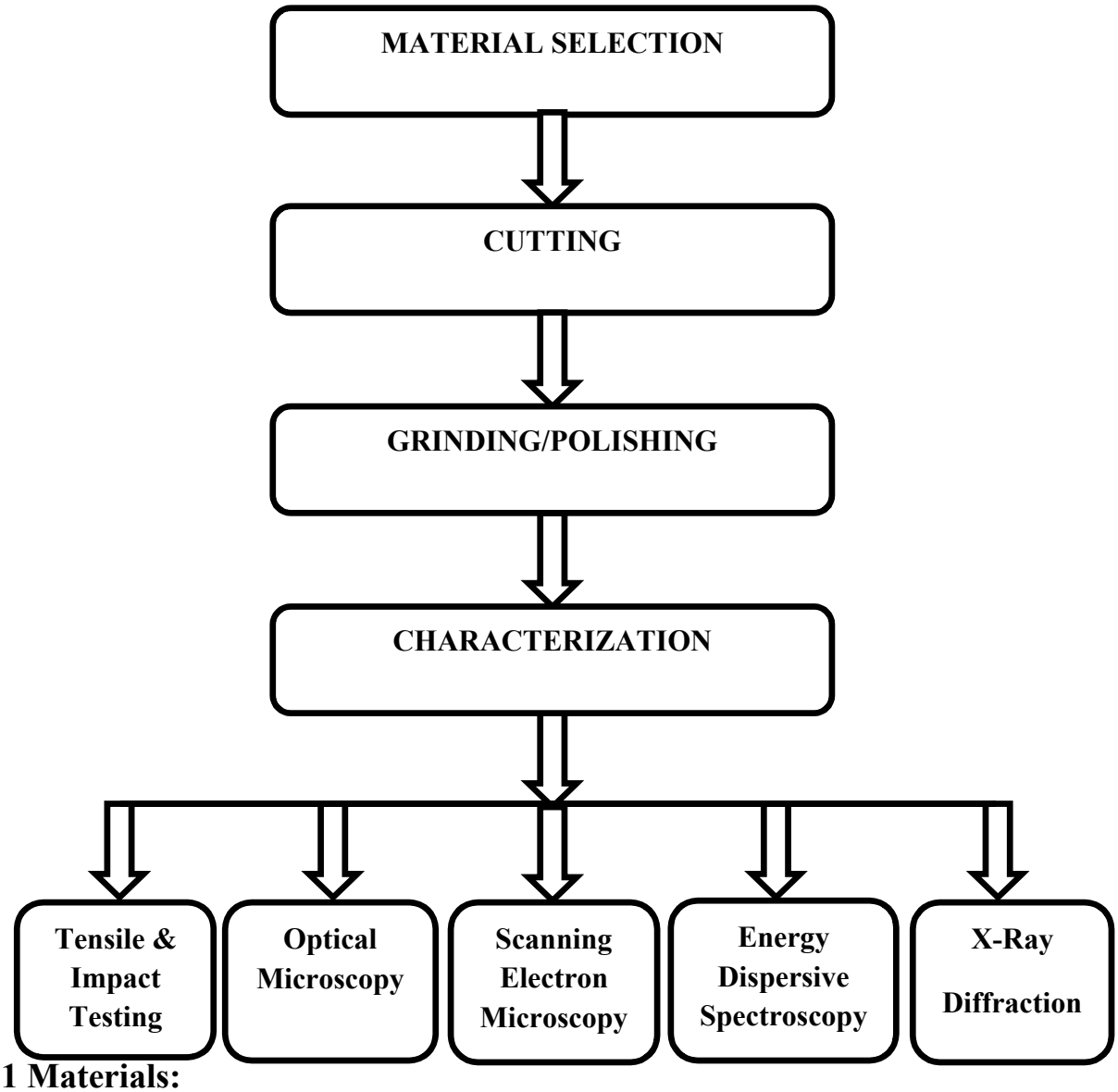

3.1 Materials:

The samples for present work were collected from Bharat Heavy Electricals Limited, Haridwar. Samples were prepared, and then these samples were subjected to mechanical and metallurgical testing techniques.

3.2 Sample preparation:

3.2.1 Cutting:

The samples of the turbine blades are cut in the transverse direction with the help of cutting machine. Different samples were obtained for further analysis.

3.2.2 Grinding and polishing:

The cut samples prepared above had an uneven surface. So the cut samples were then taken for the grinding/polishing operation. The sample was first held over a grinding machine with a moving belt to obtain a smooth surface. The grinding is done in such a way so that all the scratches are in the same direction and the grinded surface becomes flat. After this the samples are polished properly using different grits of emery paper. The sample was then polished on a fine polishing machine using an alumina polishing solution. This was done to get a well polished and a smooth surface required for further characterization of the samples. Similarly all the samples were polished for a considerable time, over and over again until a very fine and smooth surface was obtained. The polished surface was etched with Villella's etchant.

3.3 Characterization:

3.3.1 Chemical analysis:

The composition of the samples are shown in following tables

Table 3.1 Chemical composition of sample 1:

Element	C	S	P	Si	Mn	Ni	Cr	Mo	Cu	Sn	Al	Ti
Wt %	0.048	0.17	0.030	0.800	0.500	3.900	12.20	0.520	0.060	0.008	0.040	0.010

Table 3.2 Chemical composition of sample 2:

Element	C	S	P	Si	Mn	Ni	Cr	Mo	Cu	Sn	Al	Ti
Wt %	0.050	0.020	0.025	0.480	0.670	3.700	12.40	0.480	0.050	0.008	0.030	0.004

Table 3.3 Chemical composition of sample 3:

Element	C	S	P	Si	Mn	Ni	Cr	Mo	Cu	Sn	Al	Ti
Wt %	0.048	0.015	0.030	0.650	0.660	3.500	12.40	0.500	0.040	0.008	0.030	0.012

3.3.2 Hardness measurement through Brinell hardness Test:

The Brinell test is a simple indentation test for determining the hardness of a wide variety of materials. The test consists of applying a constant load (force), usually between 500 and 3000 kgf, for a specified time (10 to 30 second) using a 5 or 10 mm (0.2 or 0.4 in.) diam tungsten carbide ball on the flat surface of a work piece. The load time period is required to ensure that plastic flow of the metal has ceased. After removal of the load, the resultant recovered round impression is measured in millimeters using a low-power microscope.

Figure: 3.1 Brinell hardness tester

3.3.3 Impact testing:

V-notched Charpy testing of Experimental samples has been carried out at room temperature. The samples for this have been prepared as ASTM standard (Figure 3.2). The details of sample prepared are given in following figure:

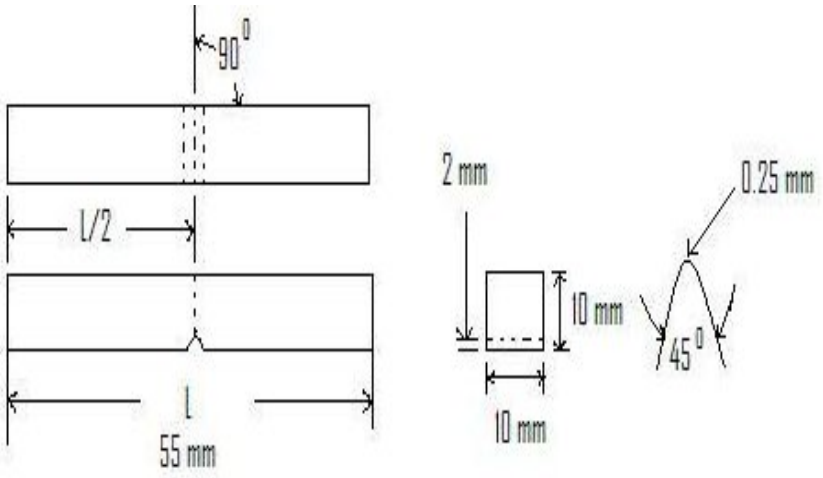

Figure: 3.2 Schematic diagram of impact sample

3.3.4 Tensile testing:

The tensile testing was carried out, using 100,000 N hydraulic-driven Universal testing Machine, for the examination of mechanical properties of experimental samples.

Cylindrical tensile specimens were prepared as per ASTM standard A 370. The details of specimen are shown below:

Figure: 3.3 Dimensional details of tensile specimen

Where,

G = gauge length = 50 mm

W = width = 12.5 mm

T = thickness = thickness of material

R = radius of fillet = 13 mm

L = overall length = 200 mm

A = length of reduced section = 60 mm

B = length of grip section = 50 mm

C = width of grip section

Figure 3.4 Tensile Tested Samples

3.3.5 Microstructural characterization through optical microscope:

The well-polished samples were then observed under an optical microscope. Micrographs were taken with the help of CCD camera attached to the optical microscope and are further viewed on

computer with optical image analyzer software at magnification of 50X to 1500X for all the sample.

3.3.6 Microstructural characterization through SEM:

Fracture surfaces of samples were examined in order to determine the exact mode of failure in the failed material. Sample have been taken from the fracture surface and observed under SEM. Extra care was taken during the cutting to avoid contamination of the fracture surface. The bottom of the sample has been flatten and then mounted on a standard base with special glue. The Scanning Electron Microscope operated at 20 kV. The Magnification of Scanning electron microscope is up to 300,000X.

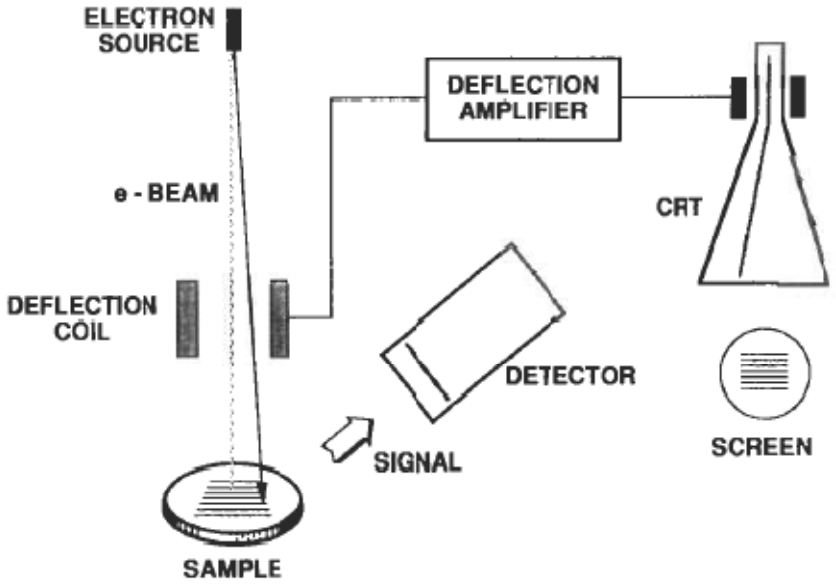

Figure: 3.6 describing operation of SEM

3.3.7 EDS (Energy Dispersive X-Ray Spectroscopy):

EDS is an extremely powerful analytical technique for identifying the existing elements present in the material. It is a technique of special value in conjunction with electron column instruments. In a few seconds a qualitative survey of the elements present in almost any sample can be made and in only a few minutes' sufficient data can be collected for quantification.

The most frequent application has been to highly polish metal samples, although non conducting samples may be studied if they can be coated with a thin conducting film.

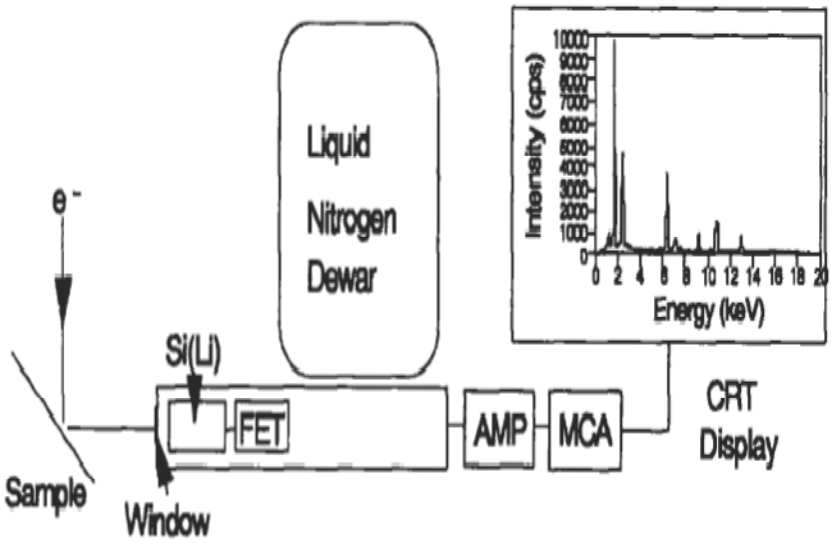

Figure: 3.7 Schematic of an EDS system on an electron column.

3.3.8: XRD Technique:

X-ray Diffraction (XRD) is a powerful technique used to uniquely identify the crystalline phases present in materials and to measure the structural properties (strain state, grain size, phase composition, preferred orientation, and defect structure) of these phases. XRD is also used to determine the thickness of thin films and multilayer's, and atomic arrangements in amorphous materials (including polymers) and at interfaces.

In XRD experiment, the diffracted intensity is measured as a function of 2θ and the orientation of the specimen, which yields the diffraction pattern. The X-ray wavelength λ is typically 0.7-2A**,** which corresponds to X-ray energies (E = 12.4 keV/A) of 6 - 17 keV.

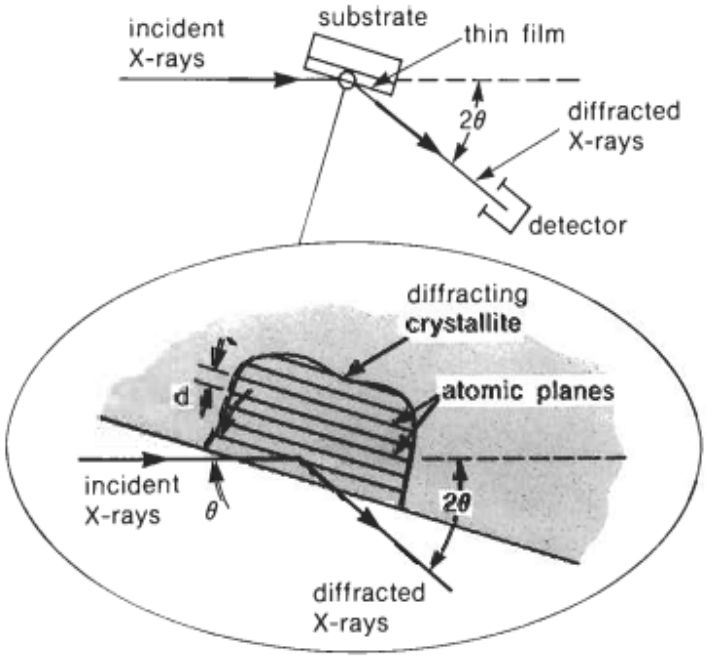

Figure: 3.8 Basic features of a typical XRD experiment

3.4 Instruments used in experiments:

The instruments used in entire process of preparation and characterizations are:

3.4.1 Instruments for chemical analysis:

- EDAX" TSL model, Advanced microanalysis solutions AMETEK, for the detection of C, N, Cr, Mn, Mo, Ni, Cu, Si, P, S, Al, Fe

3.4.2 Cutting machine:

- BAINCUT- UM Abrasive cut off machine, with coolant

3.4.3 Grinding, mounting and polishing unit:

- BAILINE Belt finishing machine (Grinder)
- BAIN MOUNT-111 Pneumatic specimen mounting press
- CHENNAI METCO wet grinding and polishing machine

3.4.4 Hardness tester:

- Brinell hardness tester

3.4.5 Microscopes:

- OLYMPUS optical microscope, model: G X 41, magnification 50X - 1000X
- LEO scanning electron microscope, model: EV 040-7636 with OXFORD NICAxsight EDS

3.4.6 XRD:

- LEO model diffractogram, with Cu Kα radiation (λ= 1.54 Å), Cu target with inbuilt Ni filter

CHAPTER 4

RESULT AND DISCUSSION

4.1 Tensile & Impact Testing Results:

Tensile and impact properties of samples were tested at room temperature and compared with standard properties of ASTM A 743 CA 6 NM. We find that properties of our samples were not according to the standard grade properties. After comparing the properties we could conclude that our all three samples have failed in the tensile and impact testing.

Table 4.1 The tensile properties of tested samples:

Sample No.	**Y.S.**	**U.T.S.**	**%E**	**%RA**	**BHN**	**IMPACT**
ASTM A 743 CA 6 NM	689	827	24	60	269	94.9
Sample 1	615	801	20	59.7	252	71,74,69
Sample 2	663	808	21.2	60.6	260	78,88,75
Sample 3	580	818	22	59.3	255	74,78,73

4.2 Microstructural Characterization:

Metallographic samples were sectioned from the blade by use of a cut-off wheel machine (ensuring water cooling during cutting). Three samples were sectioned from three different blades of same turbine. For microstructural examinations, the samples were ground and polished to a mirror like surface by use of metallographic grinding and polishing machines, respectively. The polished samples were etched using Villella's etchant for about 5–15 seconds. For SEM Analysis, the sample was cut from fractured surface of the turbine blade left and the metallographic sample was prepared until polishing stage. Microstructural characterization involved use of scanning electron microscope (SEM) and an optical microscope lined with a computerized image analyzer.

4.2.1 Microstructure and Fractographical analysis of sample 1:

The structural features of sample 1 is shown in figure 4.1(a) & 4.1(b)

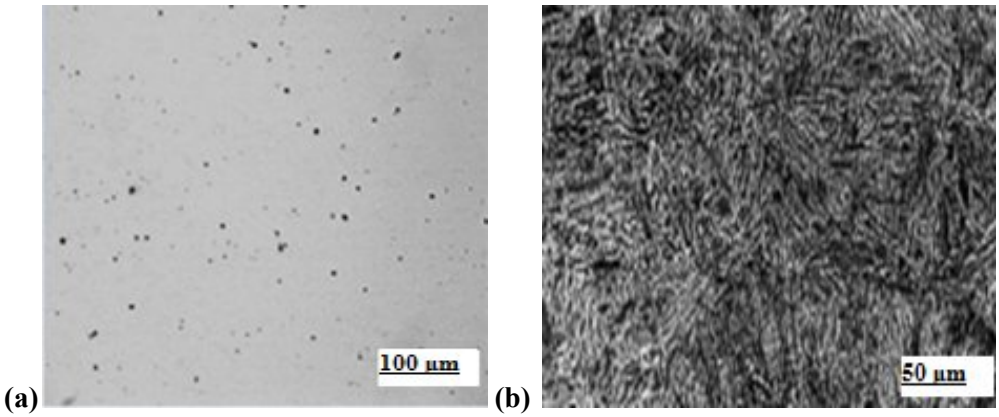

Figure 4.1 Optical micrographs of sample 1

(a) Without etched at 100x (b) Etched at 200x

Figure 4.1(a) shows the optical micrographs of unetched sample at 100x where the large number of inclusions was present. While the figure (b) of etched sample with Villella's etchant at 200x shows the tempered martensitic structure with some inclusions (dark spots).

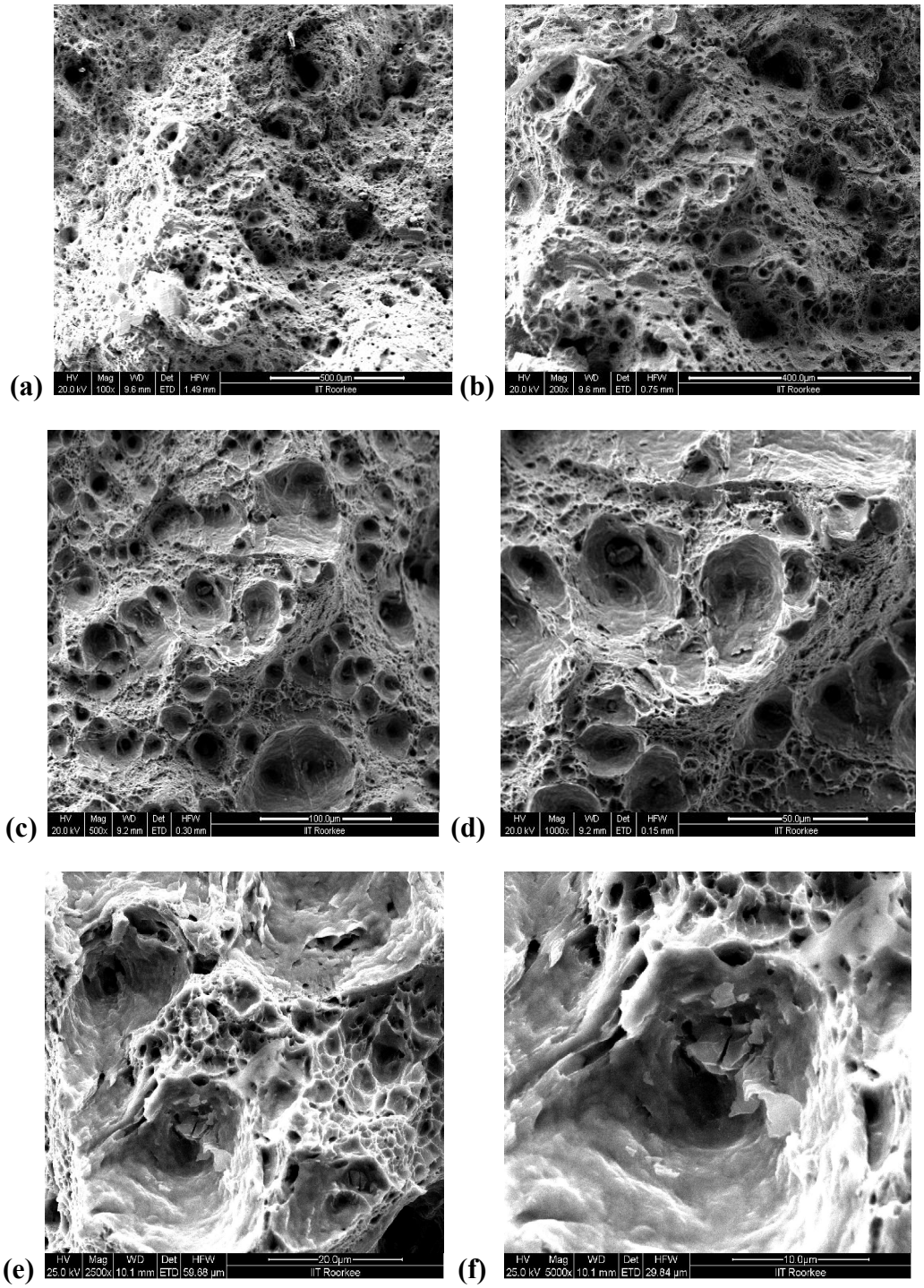

Figure 4.2 SEM micrographs of sample 1 at

(a) 100x (b) 200x (c) 500x (d) 1000x (e) 2500x (f) 5000x

From the SEM micrographs we observe that the ductile dimples are present. Figure (a) and (b) shows the large number of dimples and inclusions were present at 100x and 200x respectively. On increasing the magnification figure (c) at 500x and (d) at 1000x shows that the elongated ductile dimples with pits were present. Again increasing the magnification figure (e) at 2500x and (f) at 5000x shows the more elongated ductile dimples where inclusion can be seen easily.

4.2.2 Microstructure and Fractographical analysis of sample 2:

The structural features of sample 2 is shown in figure 4.3(a) & 4.3(b)

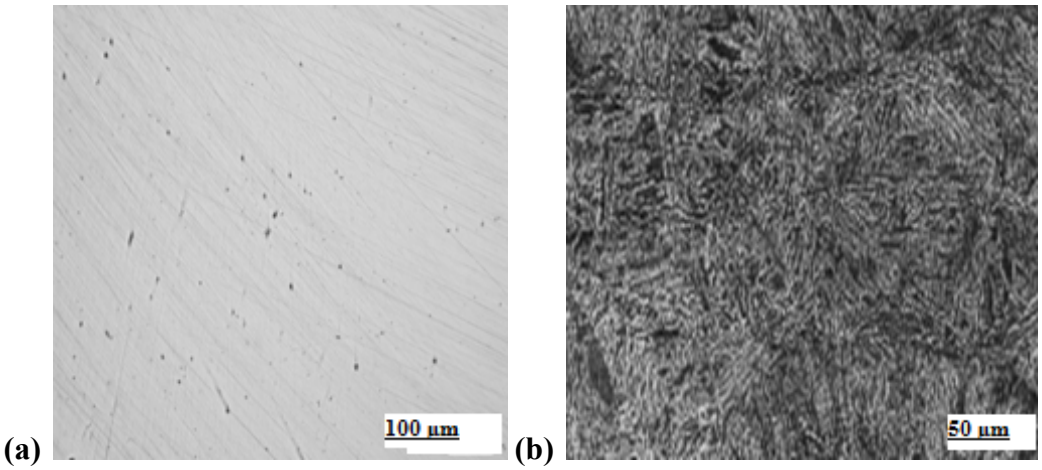

Figure 4.3 Optical micrographs of sample 2

(a) Without etched at 100x (b) Etched at 200x

The optical micrographs of unetched sample at 100x the figure (a) shows the presence of inclusions. Though the value fraction of inclusions is not much but it exhibits the features of oxide inclusion. While the figure (b) of etched sample with Villella's etchant at 200x shows the tempered martensitic structure with some inclusions and pits. These inclusions are elongated along the grain boundries.

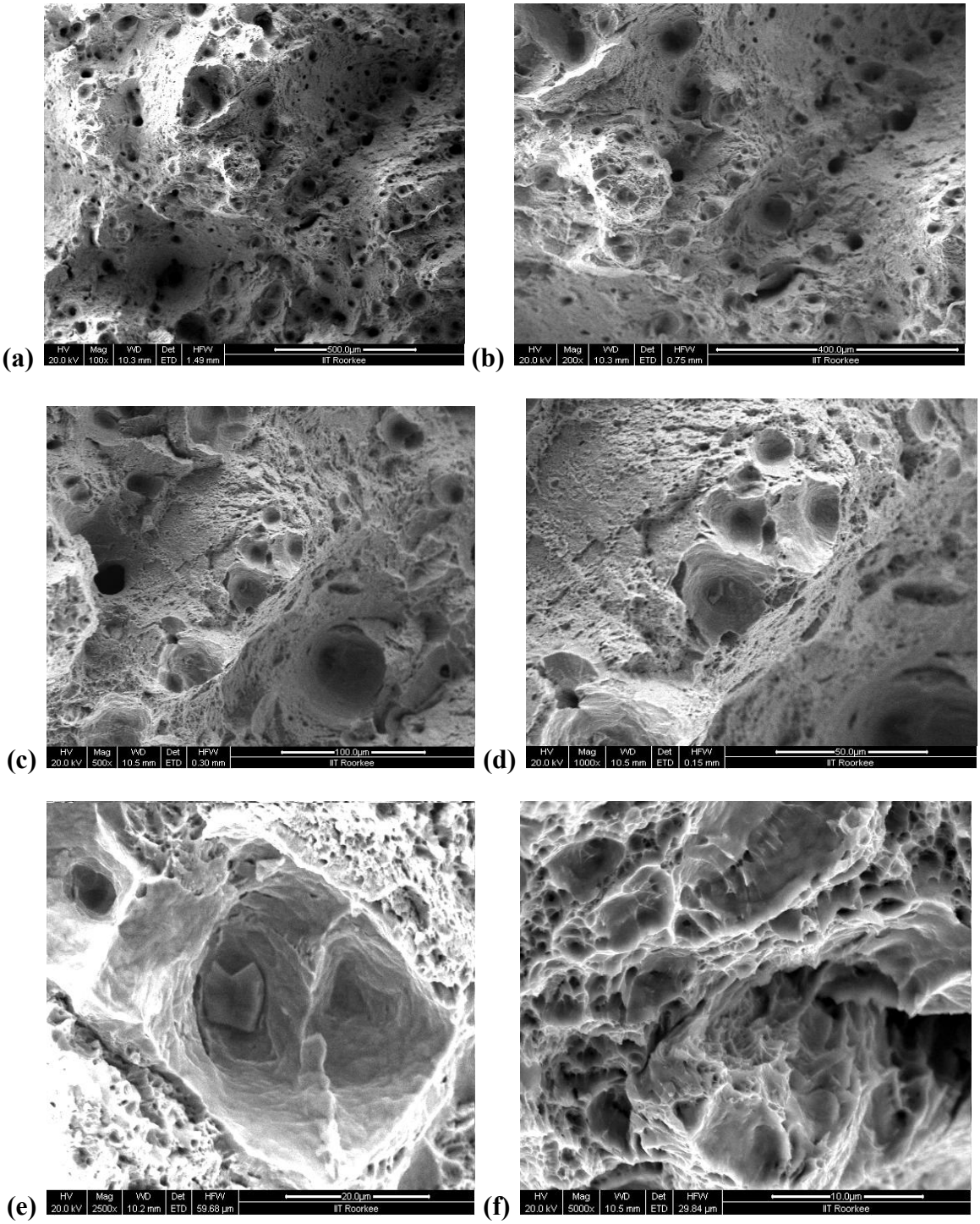

Figure 4.4 SEM micrographs of sample 2 at

(a) 100x (b) 200x (c) 500x (d) 1000x (e) 2500x (f) 5000x

From the SEM micrographs we observe that the ductile dimples are present. Figure (a) and (b) shows the large number of dimples and inclusions were present at 100x and 200x respectively. On increasing the magnification figure (c) at 500x and (d) at 1000x shows that the elongated ductile dimples with pits were present. Again increasing the magnification figure (e) at 2500x and (f) at 5000x shows the more elongated ductile dimples.

4.2.3 Microstructure and Fractographical analysis of sample 3:

The structural features of the sample 3 are shown below in figure 4.5(a) and 4.5(b).

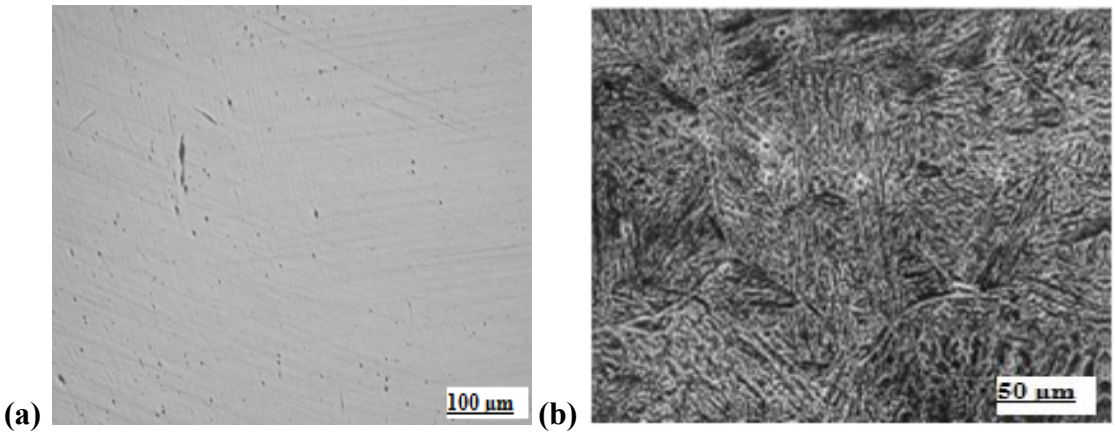

Figure 4.5 Optical micrographs of sample 3

(a) without etched at 100x (b) Etched at 200x

The optical micrographs of unetched sample at 100x as shown in figure (a) shows the presence of inclusions. While the figure (b) of etched sample with Villella's etchant at 200x shows the tempered martensitic structure with large number of inclusions and pits.

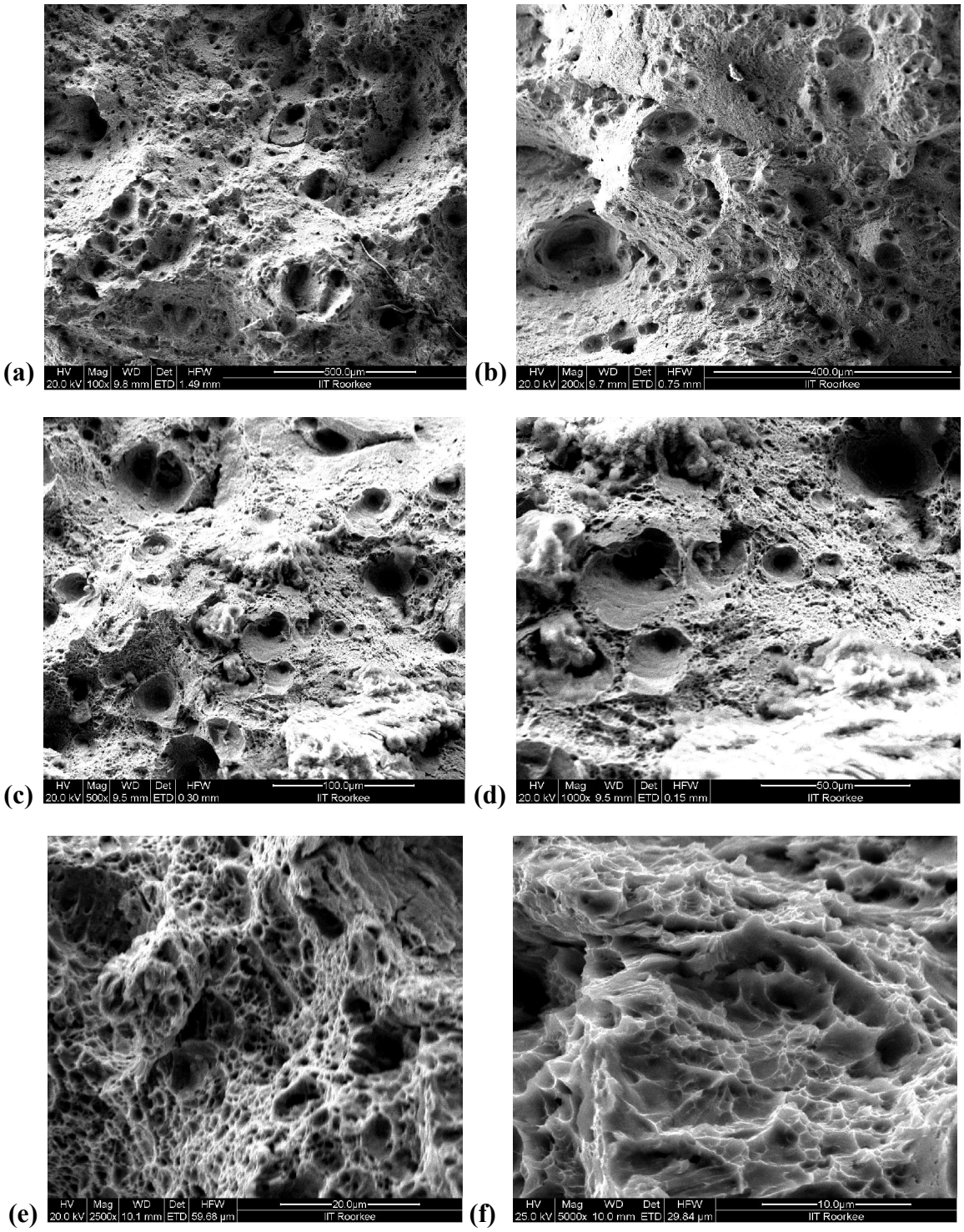

Figure 4.6 SEM micrographs of sample 2 at

(a) 100x (b) 200x (c) 500x (d) 1000x (e) 2500x (f) 5000x

From the SEM micrographs we observe that the ductile dimples were present, figure (a) and (b) shows the large number of dimples and inclusions were present at 100x and 200x respectively. On increasing the magnification figure (c) at 500x and (d) at 1000x shows that the elongated ductile dimples with pits were present. Again increasing the magnification figure (e) at 2500x and (f) at 5000x shows the more elongated ductile dimples. It is evident from the fractured surface that large number of inclusions exists inside the sample.

4.3 Energy Dispersive Spectroscopy analysis:

The Energy Dispersive Spectroscopy (EDS) analysis of the blade samples were carried out by the SEM samples at different- different magnifications and points. EDS analysis reviewed that sample contains different composition. This is presented in figure 4.7.1 to 4.7.4 for sample 1, figure 4.8.1 to 4.8.4 for sample 2 and figure 4.9.1 to 4.9.4 for sample 3. The important features obtained from this analysis are that the oxide and sulfide inclusions are present.

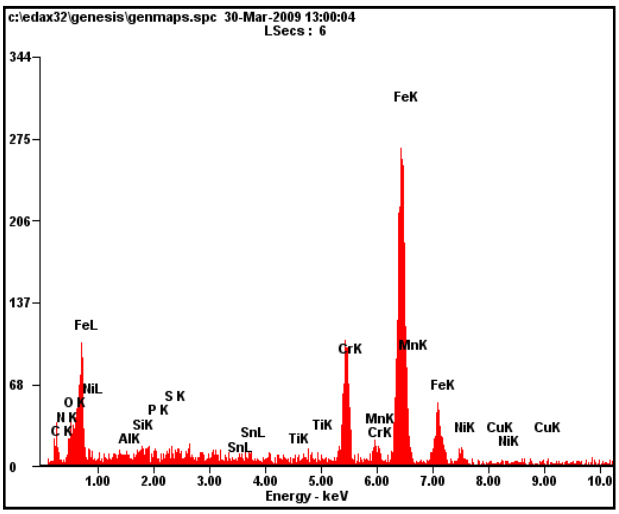

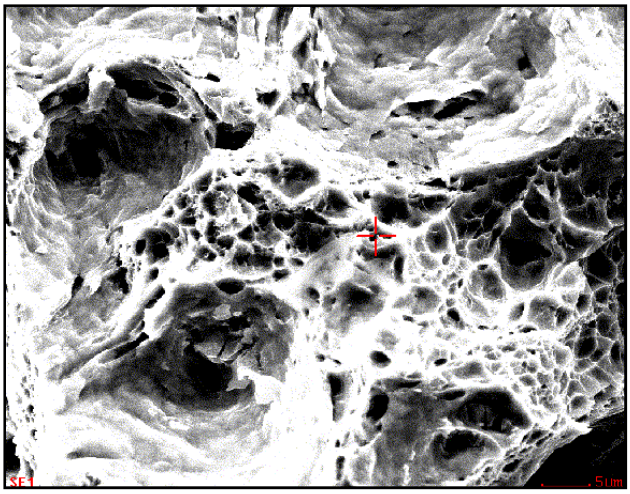

Element	*Wt%*	*At%*
CK	12.37	34.73
NK	01.50	03.62
OK	06.19	13.05
AlK	00.60	00.75
SiK	01.28	01.54
PK	00.66	00.72
SK	00.47	00.50
SnL	00.70	00.20
TiK	00.47	00.33
CrK	11.33	07.35
MnK	00.92	00.57
FeK	53.90	32.54
NiK	02.85	01.64
CuK	00.55	00.29
MoK	06.19	02.18
Matrix	Correction	ZAF

Figure 4.7.1 EDS of sample 1

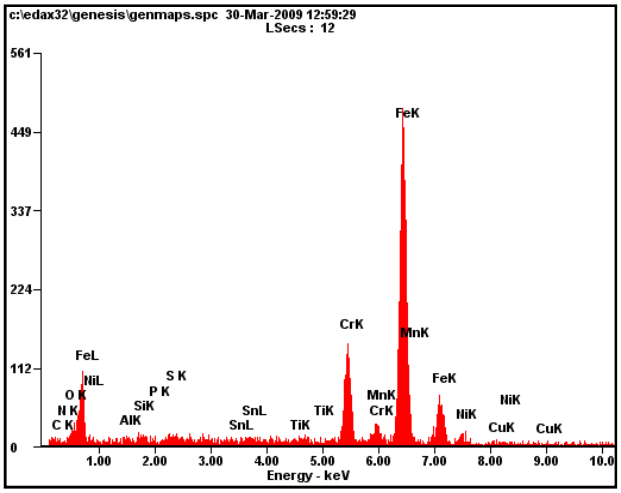

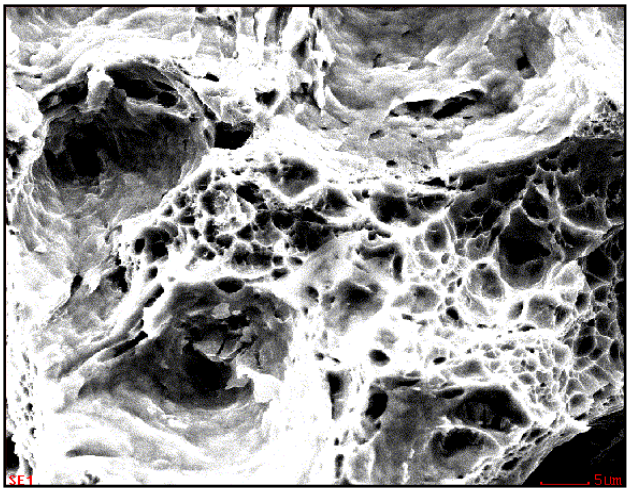

Element	*Wt%*	*At%*
CK	01.53	06.28
NK	00.67	02.35
OK	03.15	09.75
AlK	00.41	00.75
SiK	00.84	01.49
PK	00.21	00.33
SK	00.53	00.82
SnL	00.43	00.18
TiK	00.62	00.64
CrK	12.32	11.72
MnK	01.30	01.17
FeK	62.41	55.29
NiK	02.97	02.50
CuK	00.87	00.67
MoK	11.75	06.06
Matrix	Correction	ZAF

Figure 4.7.2 EDS of sample 1

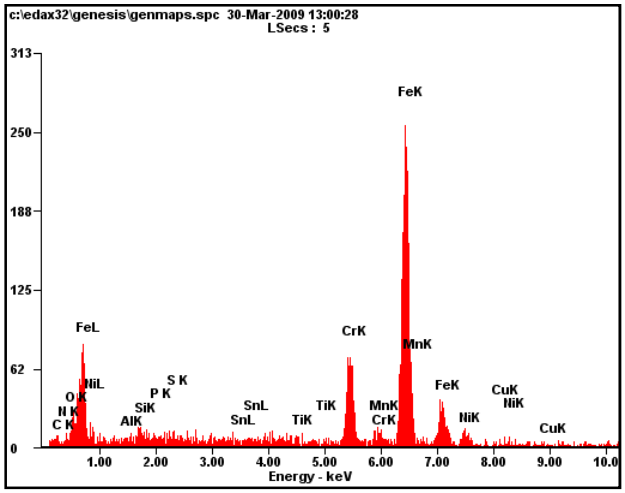

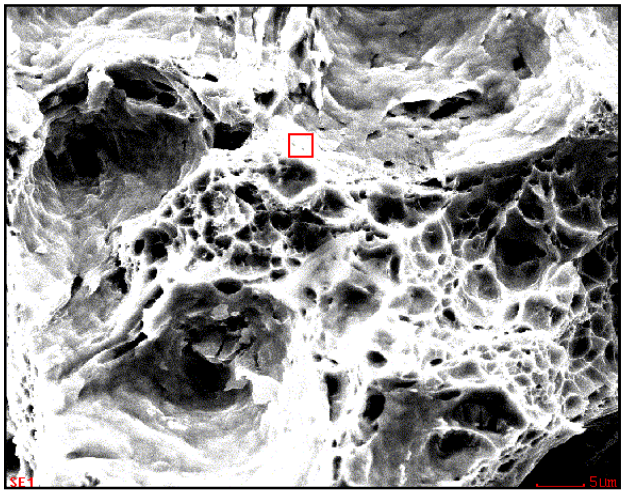

Element	*Wt%*	*At%*
CK	05.70	19.79
NK	00.93	02.77
OK	05.30	13.80
AlK	00.60	00.93
SiK	01.17	01.73
PK	00.49	00.66
SK	00.49	00.63
SnL	00.94	00.33
TiK	00.59	00.52
CrK	10.96	08.79
MnK	00.60	00.46
FeK	55.20	41.19
NiK	03.12	02.22
CuK	00.68	00.45
MoK	13.22	05.74
Matrix	Correction	ZAF

Figure 4.7.3 EDS of sample 1

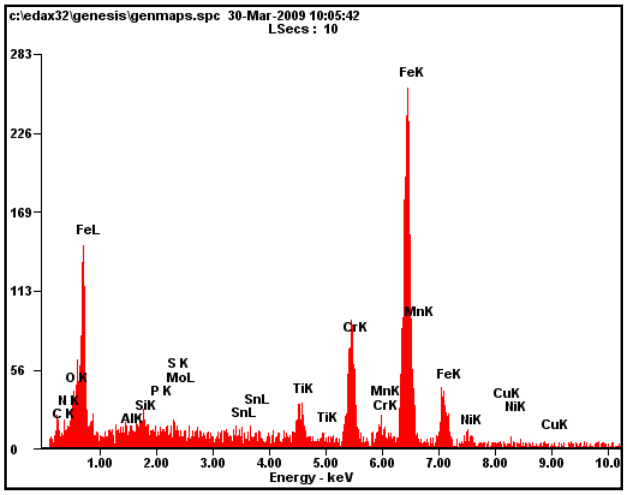

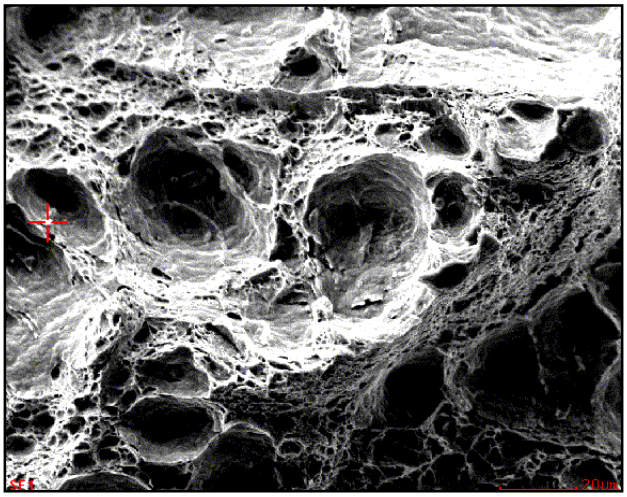

Element	*Wt%*	*At%*
CK	05.69	18.39
NK	03.44	09.53
OK	04.43	10.75
AlK	00.57	00.83
SiK	00.98	01.35
PK	00.11	00.14
MoL	01.04	00.42
SK	00.13	00.16
SnL	01.50	00.49
TiK	03.37	02.74
CrK	12.67	09.47
MnK	00.99	00.70
FeK	60.74	42.23
NiK	03.29	02.18
CuK	01.04	00.64
Matrix	Correction	ZAF

Figure 4.7.4 EDS of sample 1

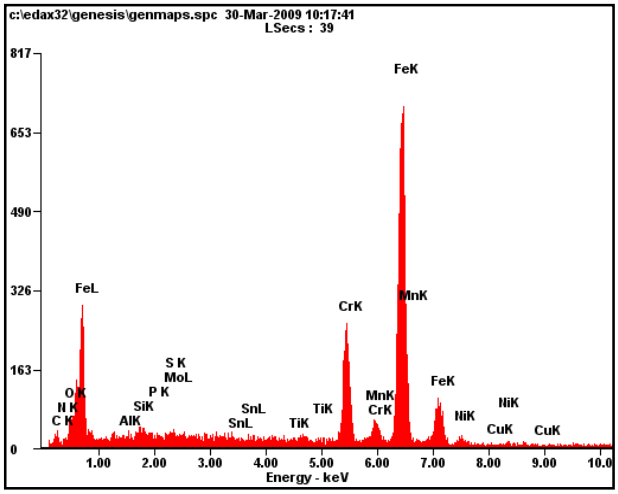

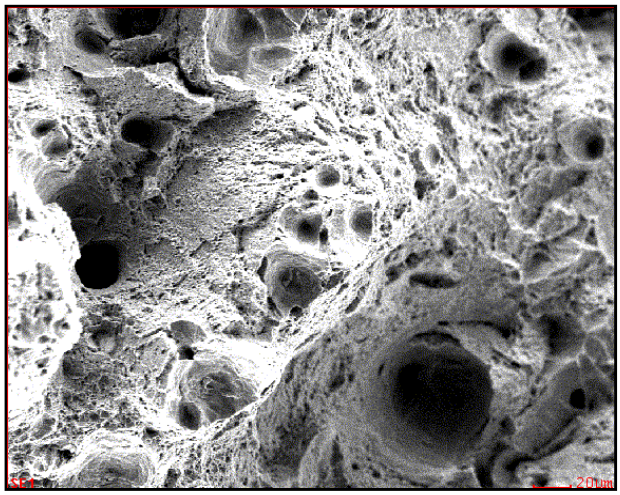

Element	*Wt%*	*At%*
CK	02.07	08.16
NK	00.76	02.58
OK	02.76	08.18
AlK	00.17	00.29
SiK	00.83	01.39
PK	00.23	00.35
MoL	01.51	00.74
SK	00.00	00.00
SnL	00.42	00.17
TiK	00.23	00.22
CrK	14.26	12.98
MnK	01.19	01.03
FeK	72.49	61.44
NiK	02.83	02.28
CuK	00.24	00.18
Matrix	Correction	ZAF

Figure 4.8.1 EDS of sample 2

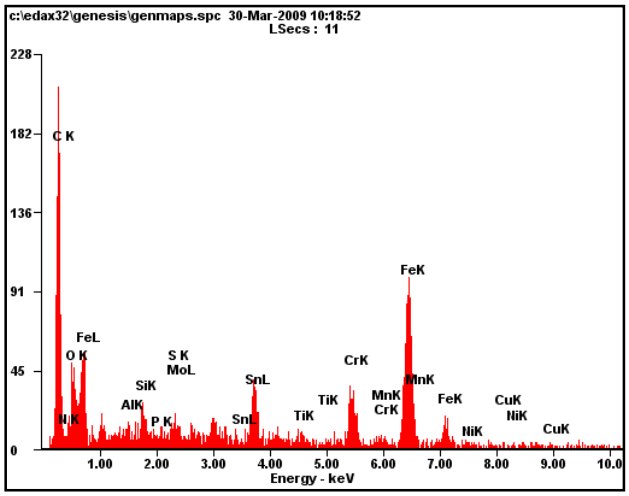

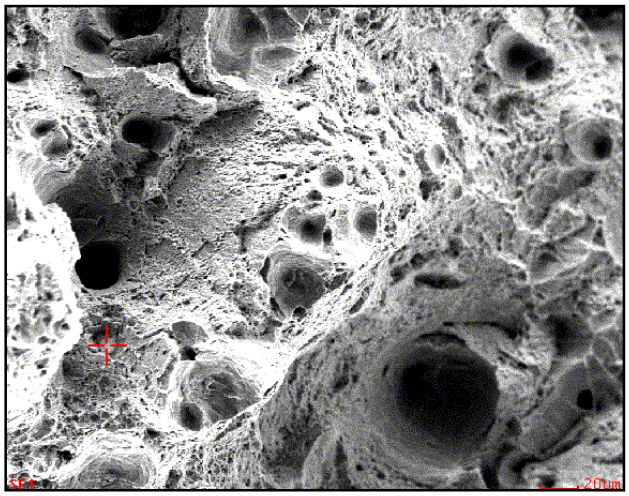

Element	*Wt%*	*At%*
CK	48.60	72.50
NK	02.36	03.02
OK	10.25	11.48
AlK	00.50	00.33
SiK	01.17	00.75
PK	00.32	00.19
MoL	01.36	00.25
SK	00.07	00.04
SnL	00.41	00.06
TiK	00.94	00.35
CrK	05.88	02.03
MnK	01.04	00.34
FeK	26.00	08.34
NiK	00.76	00.23
CuK	00.34	00.09
Matrix	Correction	ZAF

Figure 4.8.2 EDS of sample 2

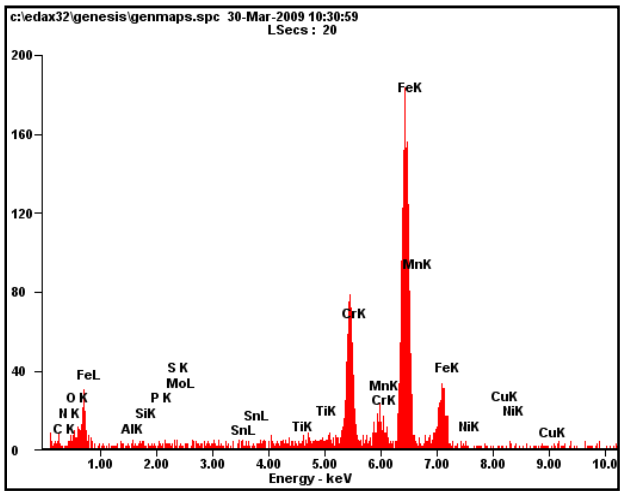

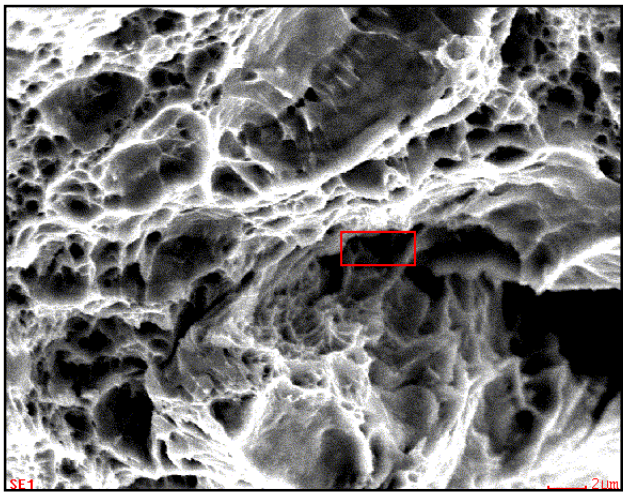

Element	*Wt%*	*At%*
CK	03.29	12.97
NK	00.49	01.67
OK	01.01	02.99
AlK	00.36	00.62
SiK	00.42	00.71
PK	00.19	00.29
MoL	00.69	00.34
SK	00.07	00.10
SnL	00.00	00.00
TiK	00.52	00.51
CrK	16.59	15.09
MnK	02.48	02.14
FeK	73.89	62.57
NiK	00.00	00.00
CuK	00.00	00.00
Matrix	Correction	ZAF

Figure 4.8.3 EDS of sample 2

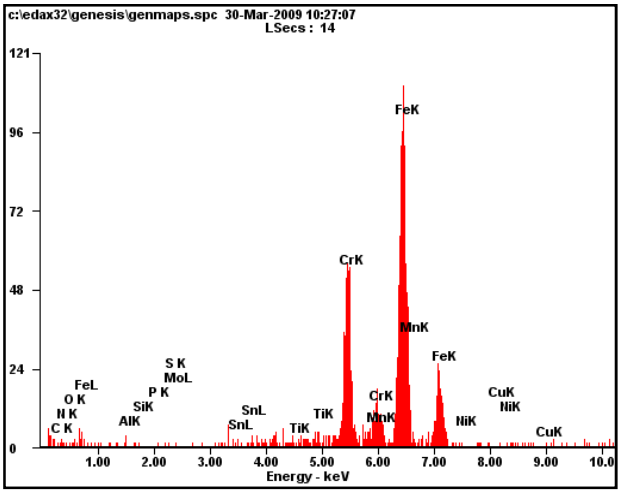

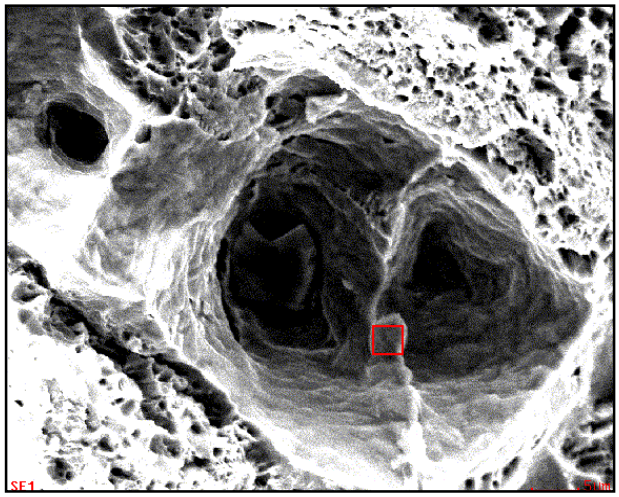

Element	*Wt%*	*At%*
CK	02.00	08.34
NK	00.47	01.67
OK	00.30	00.95
AlK	00.00	00.00
SiK	00.00	00.00
PK	00.00	00.00
MoL	00.00	00.00
SK	00.29	00.45
SnL	00.00	00.00
TiK	00.13	00.14
CrK	23.02	22.19
MnK	02.51	02.29
FeK	71.29	63.98
NiK	00.00	00.00
CuK	00.00	00.00
Matrix	Correction	ZAF

Figure 4.8.4 EDS of sample 2

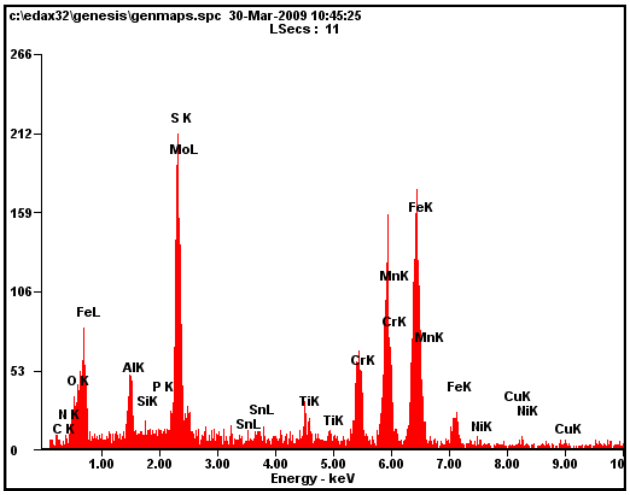

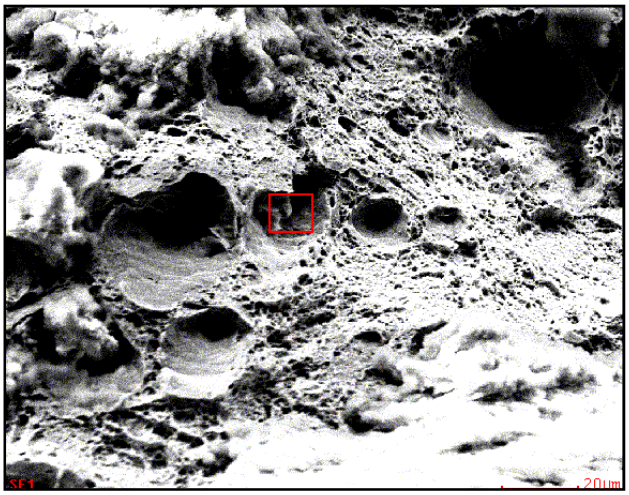

Element	*Wt%*	*At%*
CK	03.12	10.52
NK	01.36	03.94
OK	04.58	11.58
AlK	03.33	05.00
SiK	00.36	00.52
PK	00.34	00.45
MoL	05.15	02.17
SK	10.84	13.68
SnL	00.51	00.17
TiK	02.53	02.14
CrK	09.74	07.58
MnK	21.03	15.48
FeK	34.80	25.21
NiK	01.73	01.19
CuK	00.57	00.36
Matrix	Correction	ZAF

Figure 4.9.1 EDS of sample 3

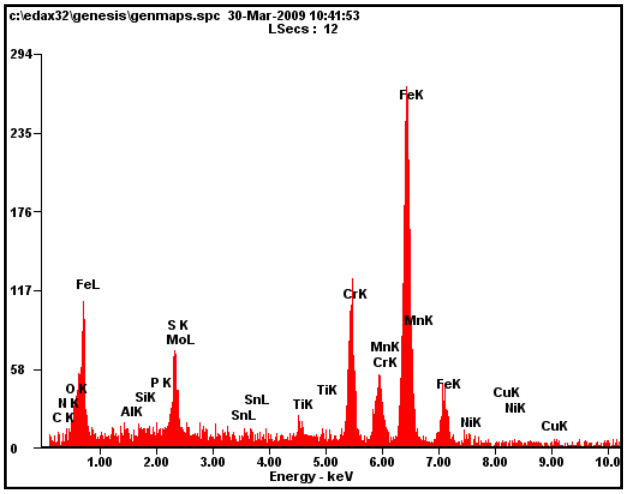

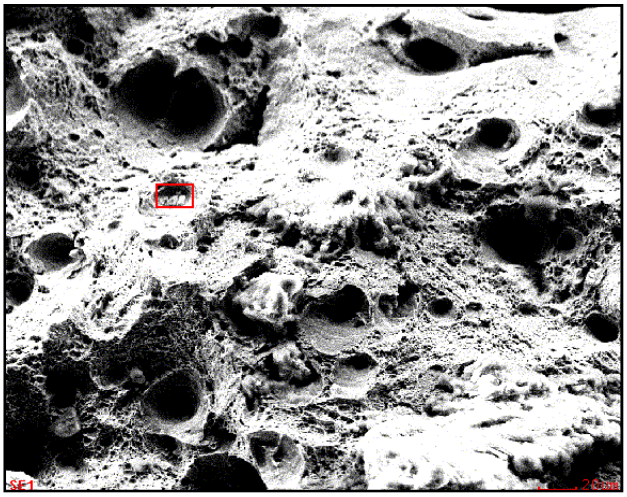

Element	*Wt%*	*At%*
CK	03.12	10.52
NK	01.36	03.94
OK	04.58	11.58
AlK	03.33	05.00
SiK	00.36	00.52
PK	00.34	00.45
MoL	05.15	02.17
SK	10.84	13.68
SnL	00.51	00.17
TiK	02.53	02.14
CrK	09.74	07.58
MnK	21.03	15.48
FeK	34.80	25.21
NiK	01.73	01.19
CuK	00.57	00.36
Matrix	Correction	ZAF

Figure 4.9.2 EDS of sample 3

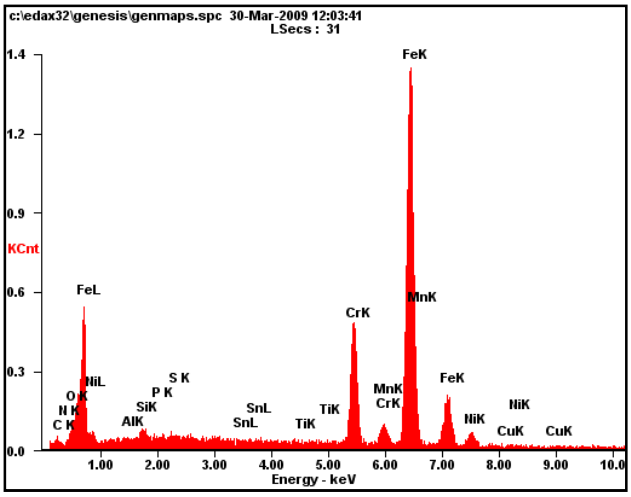

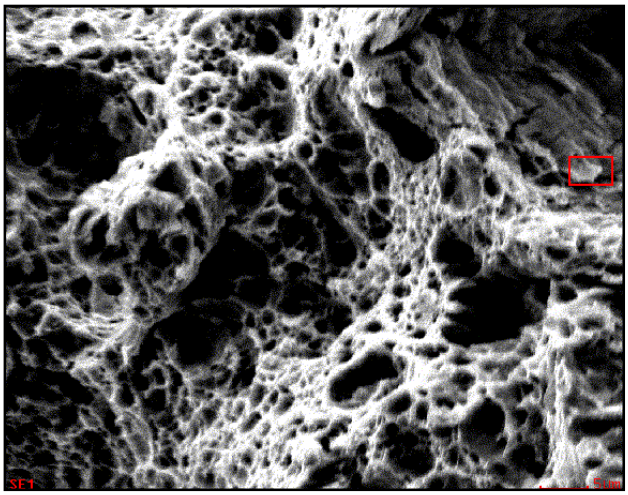

Element	*Wt%*	*At%*
CK	03.24	12.07
NK	00.32	01.03
OK	04.36	12.19
AlK	00.83	01.37
SiK	01.57	02.51
PK	00.70	01.02
SK	00.74	01.04
SnL	01.00	00.38
TiK	00.41	00.39
CrK	12.88	11.08
MnK	01.07	00.87
FeK	62.51	50.08
NiK	03.50	02.67
CuK	00.43	00.30
MoK	06.43	03.00
Matrix	Correction	ZAF

Figure 4.9.3 EDS of sample 3

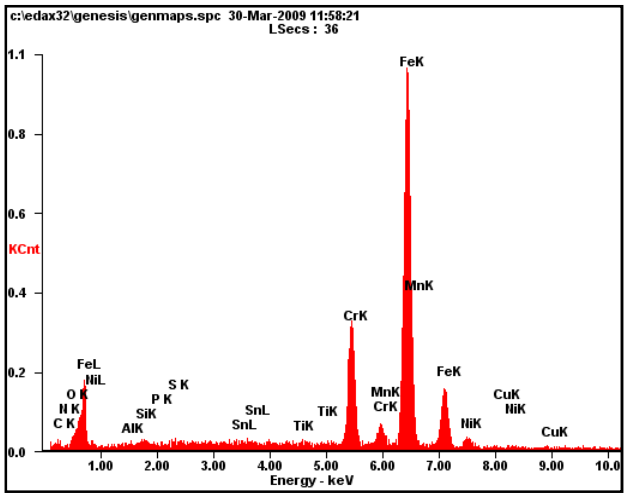

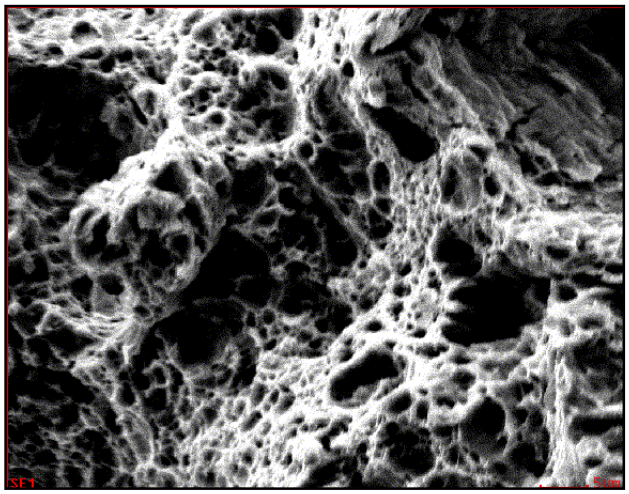

Element	*Wt%*	*At%*
CK	01.21	05.28
NK	00.00	00.00
OK	01.94	06.34
AlK	00.00	00.00
SiK	00.51	00.96
PK	00.00	00.00
SK	00.25	00.41
SnL	00.66	00.29
TiK	00.15	00.16
CrK	14.21	14.28
MnK	01.00	00.95
FeK	68.27	63.89
NiK	02.76	02.46
CuK	00.21	00.17
MoK	08.82	04.80
Matrix	Correction	ZAF

Figure 4.9.4 EDS of sample 3

4.4 X- Ray diffraction analysis:

XRD results explain the present phase and concentration, so predicted observations of each sample was described below

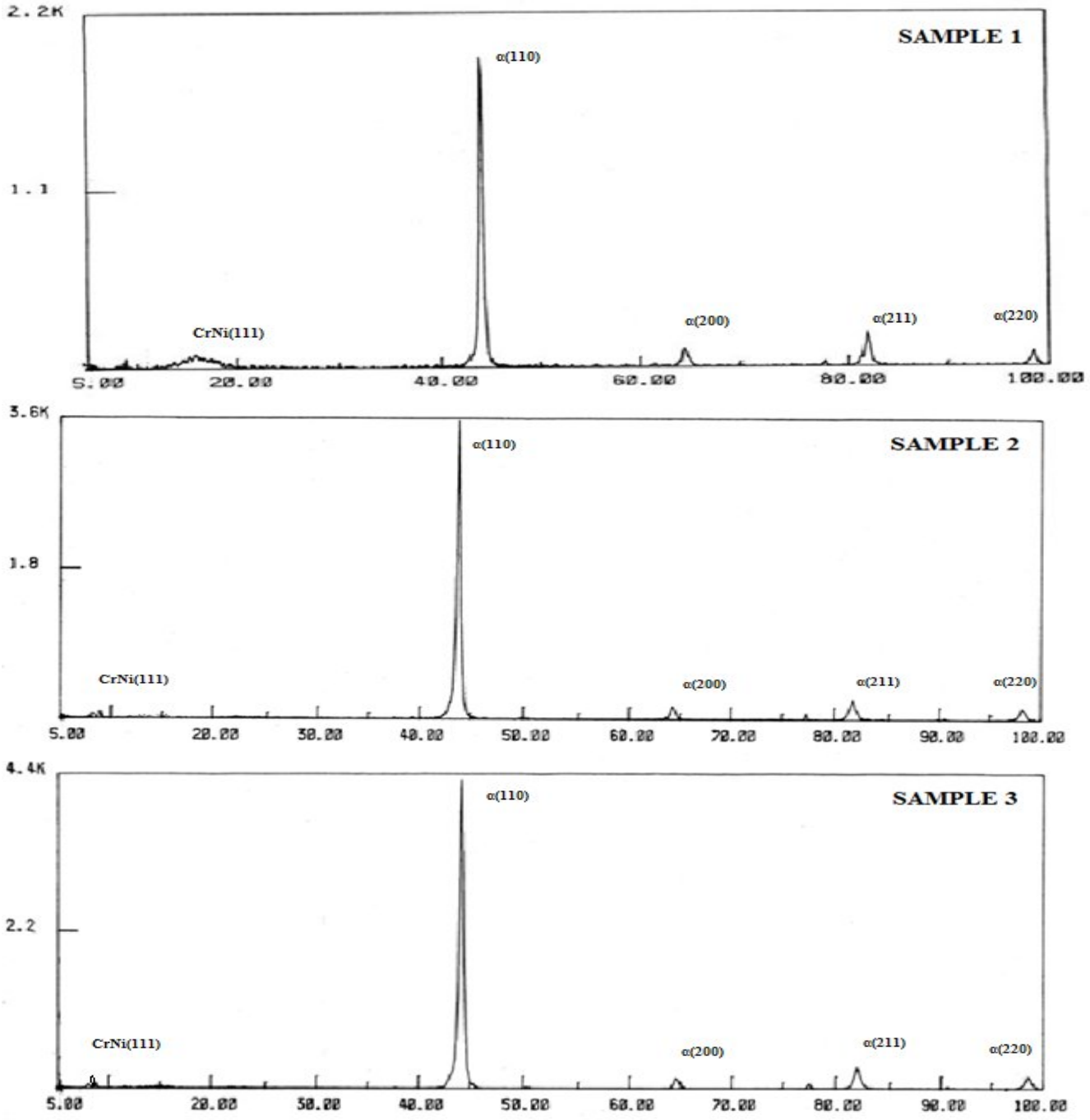

Figure 4.10 XRD pattern

From the XRD peaks of blade samples we observed that increased intensity of Iron at angle 44.67^0, 65.01^0, 82.32^0 at 98.47^0, shows the excess of Iron and remaining peaks of Cr at angle 44.37^0, 64.55^0 and 81.69^0 and Ni at angle $45.5l^0$, makes an interference pattern, are shown in three samples and shows the presence of α-phase. The α (110) at angle 44.67, α (200) at angle 65.01, α (211) at angle 82.32, and α (220) at angle 98.47^0 phases were present.

4.5 Conclusion:

The microstructural analysis of the sample revealed that the sample has tempered martensitic structure. The SEM result shows ductile dimples and inclusions. From the EDS result we can conclude that sulfide inclusions are present. The lower tensile and impact properties shows that the structural inhomogeniety. By the above analysis we can conclude that main cause of failure is the sulfide inclusion which shows the casting defect.

REFERENCES

1. http://www.britannica.com/EBchecked/topic/444719/Sir-Charles-Algernon-Parsons
2. Turbine. Encyclopaedia Britannica Online
3. A new look at Heron's 'steam engine'" (1992-06-25). Archive for History of Exact Sciences 44 (2): 107-124.
4. O'Connor, J. J.; E. E. Roberston (1999). Heron of Alexandria. MacTutor.
5. Ahmad Y Hassan (1976). Taqi al-Din and Arabic Mechanical Engineering, p. 34-35. Institute for the History of Arabic Science, University of Aleppo.
6. http://www.birrcastle.com/steamTurbineAndElectricity.asp
7. http://www.universityscience.ie/pages/scientists/sci_charles_parsons.php
8. http://www.birrcastle.com/steamTurbineAndElectricity.asp
9. Parsons, Sir Charles A.. "The Steam Turbine". http://www.history.rochester.edu/steam/parsons/part1.html
10. ASM, Metals Handbook: Casting, Vol. 15, 9th ed., Materials Park, OH, P 1583-1607, 1988.
11. ASM, Metals Handbook: Fractography, Vol. 12, 9th ed., Materials Park, OH, P 34-40, 1987.
12. Le May, Metallography in Failure Analysis, J.L. McCall and P.M. French, Ed., American Society for Metals, 1977.
13. C.D. Beachem and D.A. Meyn, “Electron Fractography”, STP 436, American Society for Testing and Materials, 1968, P 59.
14. Hyojin Kim” Study of the fracture of the last stage blade in an aircraft gas turbine” Engineering Failure Analysis (2009).
15. Zainul Huda “Metallurgical failure analysis for a blade failed in a gas-turbine engine of a power plant” Materials and Design 30 (2009) P 3121–3125.
16. J. Kubiak Sz *, J.A. Segura, G. Gonzalez R, J.C. García, F. Sierra E, J. Nebradt G, J.A. Rodriguez “Failure analysis of the 350MW steam turbine blade root” Engineering Failure Analysis 16 (2009) P 1270–1281.
17. Haijun Tang *, Dashu Cao, Hongyu Yao, Mingli Xie, Ruichun Duan “Fretting fatigue failure of an aero engine turbine blade” Engineering Failure Analysis 16 (2009).
18. J. Kubiak, G. Urquiza, J.A. Rodrigueza, G. González, I. Rosales, G. Castillo, J. Nebradt “Failure analysis of the 150MW gas turbine blades” Engineering Failure Analysis 16 (2009) P 1794–1804.

19. Z. Mazur, R. García-Illescas, J. Porcayo-Calderón "Last stage blades failure analysis of a 28 MW geothermal turbine" Engineering Failure Analysis 16 (2009) P 1020–1032.
20. Seon-gab Kim, Young-ha Hwang, Tae-gu Kim, Chang-min Shu " Failure analysis of J85 Engine turbine blades" Engineering Failure Analysis 15 (2008) P 394–400.
21. E. Poursaeidi, M. Aieneravaie, M.R. Mohammadi "Failure analysis of a second stage blade in a gas turbine engine" Engineering Failure Analysis 15 (2008) P 1111–1129.
22. Mehdi Tofighi Naeem, Seyed Ali Jazayeri, Nesa Rezamahdi " Failure Analysis of Gas Turbine Blades" *The 2008 IAJC-IJME International Conference ISBN 978-1-60643-379-9.*
23. Zi-Li Xu, Jong-Po Park, Seok-Ju Ryu "Failure analysis and retrofit design of low pressure 1st stage blades for a steam turbine" Engineering Failure Analysis 14 (2007) P 694–701.
24. Zhi-wei, Yu Xiao-lei, Xu Shu-hua, Liu Yu Li "Failure Investigation on Failed Blades Used in a Locomotive Turbocharger" J Fail. Anal. and Preven. 7 (2007) P 386–392.
25. Wei-Ze Wang, Fu-Zhen Xuan, Kui-Long Zhu, Shan-Tung Tu" Failure analysis of the final stage blade in steam turbine" Engineering Failure Analysis 14 (2007) P 632–641.
26. H. Sepehri amin, a. Kermanpur, s. Ziaei rad, h. Farhangi, m. Mosaddeghfar "An investigation on failure analysis of Titanium gas turbine compressor blade" prooceedings of 8th international fracture conference 7 – 9 november 2007 istanbul (turkey).
27. N. Vardar a,*, A. Ekerim "Failure analysis of gas turbine blades in a thermal power plant" Engineering Failure Analysis 14 (2007) P 743–749.
28. A.P. Tschiptschin , C.R.F. Azevedo "Failure analysis of turbo-blower blades" Engineering Failure Analysis 12 (2005) P 49–59.
29. J. Kubiak Sz., G. Gonzalez R., D. Juarez R., J. Nebradt G., and F. Sierra E." An Investigation on the Failure of an L-0 Steam Turbine Blade" Journal of Failure Analysis and Prevention Volume 4(3) June 2004.

30. Goutam Das, Sandip Ghosh Chowdhury, Ashok Kumar Ray, Swapan Kumar Das, Deepak Kumar Bhattacharya “Turbine blade failure in a thermal power plant” Engineering Failure Analysis 10 (2003) P 85–91.
31. Myounggu Park, Young-Ha Hwang, Yun-Seung Cho, Tae-Gu Kim “Analysis of a J69-T-25 engine turbine blade fracture” Engineering Failure Analysis 9 (2002) P 593–601.